FE-2341-4
Distribution Categories UC-90g and UC-93

# A HIGH MAGNETIC FIELD MHD GENERATOR PROGRAM

Quarterly Report for the

Period July, 1977 - September, 1977

Submitted by

Profs. R. H. Eustis, C. H. Kruger and M. Mitchner,
Adjunct Prof. S. A. Self, and Dr. J. K. Koester



December, 1977



Contract No. EX 76-C-01-2341

PREPARED FOR
THE UNITED STATES DEPARTMENT OF ENERGY

High Temperature Gasdynamics Laboratory
Department of Mechanical Engineering
Stanford University

---

## Forward

Much of the work on this program is carried out by student Research Assistants and High Temperature Gasdynamics Laboratory staff members in addition to the Principal Investigators. The additional persons involved in a major way with the work reported here are

Dr. Takashi Nakamura
Mr. John P. Barton
Mr. Bradford Bennett
Mr. Kent James
Mr. Marion Jenkins
Mr. Ralph Kowalik
Mr. Roy R. Rankin
Mr. William C. Unkel

Table of Contents

List of Tables

List of Figures

List of Figures

ABSTRACT

As part of the study of the influence of non-uniformities on MHD generator performance a theory was evolved which treats the MHD generator as a boundary value problem with the ocscillation frequency determined by the boundary oscillation (such as a combustor). The results are in good agreement with data reported in earlier reports. A laser fluorescence temperature measuring technique was developed which was tested on a bunsen burner. The technique provides for 3-dimensional spatial resolution of temperature. Further analysis of the sidewall boundary layer velocity profile data provided elucidation of turbulence damping in the boundary layer. The turbulence level was reduced by about 20 percent by the magnetic field of 2.4 tesla. Careful experiments were made to measure Joule heating effects in the electrode boundary layer. Preliminary reduction of the data showed a temperature and electron density elevation due to Joule heating. Thermal tests were made of disk generator construction techniques which utilizes metallized MgO ceramics soldered or brazed to a copper substrate.

## 1.0 OBJECTIVE AND SCOPE OF WORK

The objective of the program is to investigate the high magnetic field effects in MHD channels which will influence the design of large scale generators. The work includes the study at high fields of 1) plasma non-uniformities and instabilities and 2) boundary layer and Hall field phenomena. In addition a third activity is centered on the existing Stanford 6 tesla magnet where small scale linear and disk channels are investigated.

## 2.0 SUMMARY OF PROGRESS TO DATE

The tasks of the contract statement of work have been grouped into three Work Areas as shown in Table 1, Milestones for MHD Research at High Magnetic Fields. The Work Areas which are keyed to the program objectives are

I Plasma Nonuniformities and Instabilities

II Boundary Layer and Hall Field Phenomena

III Six Tesla Magnet Investigations

In Work Area I, significant progress has been made in understanding the pressure fluctuation data and a new temperature measuring technique which provides 3-dimensional spatial resolution has been developed.

Measurements made in Stanford's M-2 MHD facility have shown that significant increases in inherent pressure fluctuation levels can take place within a generator under operation at sufficiently high current densities and applied magnetic fields. Although these findings are in qualitative accord with early magnetoacoustic theories several particular features of the experimental results appear to differ from the predictions of the theories. In the initial theories dealing with the magnetoacoustic instability the equations were linearized and the wavenumber was taken to be an independent variable, so that the results apply to the initial value problem of the time development of a small disturbance within an infinite plasma. Such a solution would perhaps apply to the description of electro-magnetic effects in an operating generator or small scale inherent fluctuations. Fluctuations in a real generator can be driven by disturbances originating in the combustor and so the boundary value problem provides a more appropriate model. The results of this type of analysis using parameters which correspond to the low velocity conditions of the M-2 experiment show the theory in good agreement with experimental observations.

Recent work on spatially resolved temperature measurement has focused on the development of a laser fluorescence diagnostic. The technique uses a cw dye laser to pump a transition between two excited levels of sodium which is seeded in the combustion gases. An enhanced spontaneous emission signal from the upper level (fluorescence) is observed along a line of sight perpendicular to the exciting laser beam. This signal can thus be spatially resolved to the small volume intersected by the laser beam and the collection line of sight.

In Work Area II, further work has been done in analyzing the data obtained during the sidewall boundary layer experiment and a series of experiments was made to investigate Joule heating near the electrodes. Measurements of the insulating wall velocity profiles using laser anemometry were reported in the last Quarterly Report. Further analysis of the laser anemometry data has yielded turbulence intensity profiles for the three generator conditions tested. The data clearly indicate that turbulence damping was present with an average value of approximately 0.8. A series of runs was performed to measure temperatures and electron number densities in an electrode wall boundary layer. The purpose of the experiments was to observe electron non-equilibrium in the inner regions of the boundary layer, and to measure the effects of Joulean heating on the temperature and electron number density profiles. Although the data for the experiment are still being reduced, some preliminary results indicated the temperature profile with current to be considerably steeper near the wall than the profile without current. This will cause substantial changes in wall heat transfer and boundary layer voltage drops.

In Work Area III, progress was made in both the disk and linear generator program. Efforts were directed toward the construction of the six tesla disk generator experimental facility and toward the analytical studies to predict the performance of the present disk generator facility and to assess the applicability of the disk generator to the commercial MHD power plant. The main components of the disk generator experimental facility underwent a series of thermal tests for a total operation time of 4 hours. The disk generator insulator plates constructed with metalyzed $M_gO$ ceramics were tested extensively. Study of the boundary layer and the investigation of the current discharge structure in the disk generator configuration were initiated. The computer codes to predict the performance of the disk generator experimental facility are being developed. The study to predict the performance and to assess the applicability of the disk generator to the commercial MHD power plant was started.

Work on the linear configuration centered around channel design. Tests were conducted to test the peg wall concept, a channel configuration was decided upon, and a preliminary test was conducted on a possible electrode material.

The status of the work is summarized in the program milestone chart, Figure 1.

Table 1

Milestones for MHD Research at High Magnetic Fields

WORK AREA I - Plasma Nonuniformities and Instabilities

Task 1 Plasma nonuniformity study

- 1.1 Initiate development of pressure fluctuation diagnostics
- 1.2 Test of diagnostics in cold channel
- 1.3 Test of diagnostics of M-2 channel
- 1.4 Test of diagnostics in Super M-8 channel

Task 2 Development of temperature fluctuation diagnostics

- 2.1 Initiate bench development of rapid line reversal method
- 2.2 Apply rapid line reversal method to open burner
- 2.3 Apply rapid line reversal method to M-8 channel
- 2.4 Bench development of laser system for spatial resolution
- 2.5 Apply laser system to open burner
- 2.6 Apply laser system to M-8 channel

Task 3 Instabilities

- 3.1 Tests of fluctuation in cold channel (see 1.2)
- 3.2 Initiate test with normal operating conditions in M-2
- 3.3 Initiate test with introduced disturbances in M-2
- 3.4 Begin tests in Super M-8

WORK AREA II - Boundary Layer and Hall Field Phenomena

Task 4 Boundary layer study

- 4.1a Develop LDV techniques
- 4.1b Develop line intensity techniques
- 4.1c Develop line reversal techniques
- 4.1 Initiate development of technique for remote channel operation
- 4.2 Develop access in mock-up of Super M-8 channel
- 4.3 Test of electrode boundary layer in Super M-8 channel
- 4.4 Extend theory to large MHD channels
- 4.5 Complete fabrication of M-8 channel

Task 5 Turbulence damping study

- 5.1 Measurement of turbulence intensity (part of test listed in 4.3)

Table 1 (Continued)

Milestones for MHD Research at High Magnetic Fields

Task 6 Hall field limitation study

- 6.1 Initiate electrode development for Super M-8 channel
- 6.2 Apply field test in Super M-8 channel outside of magnet

Task 7 Electrode configuration study

- 7.1 Electrode development in channel mock-up
- 7.2 Preliminary test of electrode in M-2 channel
- 7.3 Test in Super M-8 channel

Task 8 Current concentration

- 8.1 Initiate development of segmented electrode
- 8.2 Test segmented electrode in M-2 channel
- 8.3 Test segmented electrode in Super M-8 channel

WORK AREA III - Six Tesla Magnet Investigations

Task 9 Disk generator program

- 9.1a Complete construction of disk generator
- 9.1b Complete construction of disk generator exhaust system
- 9.2 Thermal checkout of disk system
- 9.3 Test in 6 tesla magnet

Task 10 Linear 6 tesla channel

- 10.1 Complete design of linear channel for 6 tesla magnet
- 10.2 Complete construction of linear channel
- 10.3 Thermal test outside of magnet
- 10.4 Experiment in 6 tesla magnet with clean fuel
- 10.5 Test in 6 tesla magnet with coal combustion

HIGH MAGNETIC FIELD
MHD GENERATOR PROGRAM
Technical Work Areas

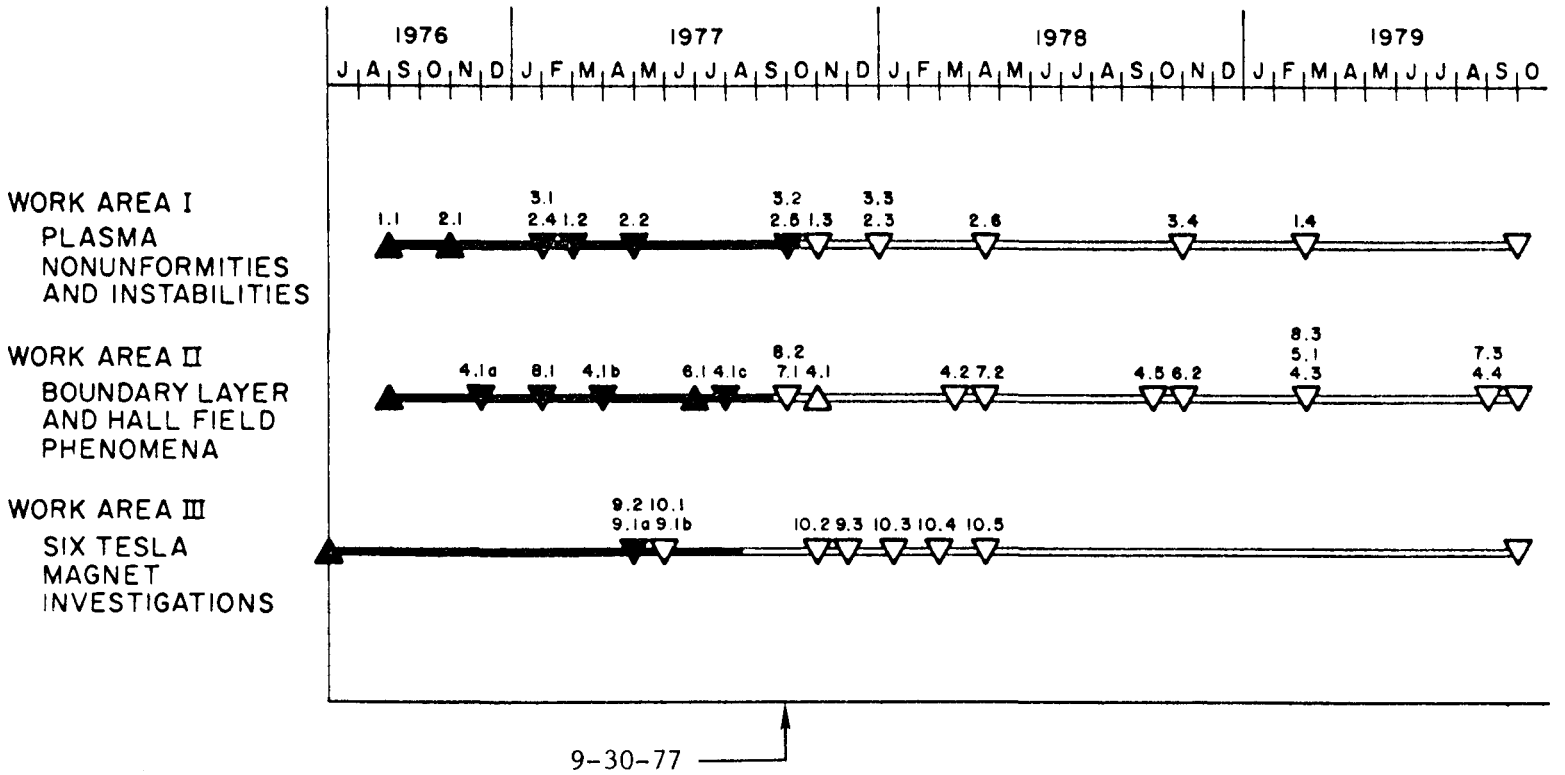


Figure 1. Program Milestone Chart.

## 3.0 DESCRIPTION OF TECHNICAL PROGRESS

### 3.1 Work Area I - Plasma Nonuniformities and Instabilities

#### 3.1.1 Plasma Instability Investigations

Measurements made in Stanford's M-2 MHD facility have shown that significant increases in inherent pressure fluctuation levels can take place within a generator under operation at sufficiently high current densities and applied magnetic fields (see Fig. 2). Although these findings are in qualitative accord with early magnetoacoustic theories (see, for example, J.E. McCune, "Wave Growth and Instability in Partially Ionized Gases," Int. Symp. on MHD Electrical Power Generation, Paris, 1964) several particular features of the experimental results appear to differ from the predictions of the theories. The theories predict, for example, appreciable damping of inherent property fluctuations for the case of an applied magnet field and zero steady-state current (as a result of the $\vec{j} \times \vec{B}$ braking force acting on fluctuation currents). Also significant growth is predicted for the case of no applied magnetic field with current only (as a result of ohmic heating effects). As indicated in Figures 2 and 3, the data show that either the presence of a steady-state current or an applied magnetic field alone have a negligible effect on the pressure fluctuation levels. Early magnetoacoustic theories also predict, to first order, that the growth in fluctuation levels should be frequency (or wavelength) independent. The frequency spectra of Figure 3 show, however, that the observed growth in fluctuation levels occurs primarily in a low frequency ($\lesssim$ 100 Hz) range.

In the initial theories dealing with the magnetoacoustic instability the equations were linearized and the wavenumber was taken to be an independent variable, so that the results apply to the initial value problem of the time development of a small disturbance within an infinite plasma. Such a solution would perhaps apply to the description of electro-magnetic effects in an operating generator on small scale inherent fluctuations.

Fluctuations in a real generator can be driven by disturbances originating in the combustor and so the boundary value problem, as shown in Figure 4 for an ideal Faraday generator, provides a more appropriate model. In this approach the internal properties oscillate at the excitation frequency of the boundary and so the frequency is treated as an independent variable. Linearization theory provides a dispersion relation which yields three traveling waves as solutions. Two of these, the forward and backward "magnetoacoustic" waves, correspond in the appropriate limit to normal acoustic waves. The third root, termed the "magnetoentropic" wave, corresponds to the little discussed entropy wave of normal linearized fluid mechanics. The entropy wave is essentially a small scale temperature (or entropy) disturbance which is convected with the fluid. The general solution for a disturbance of specified frequency in the generator is then a linear combination of these three waves and the constant coefficients are determined from the imposition of boundary conditions, such as shown in Figure 4.

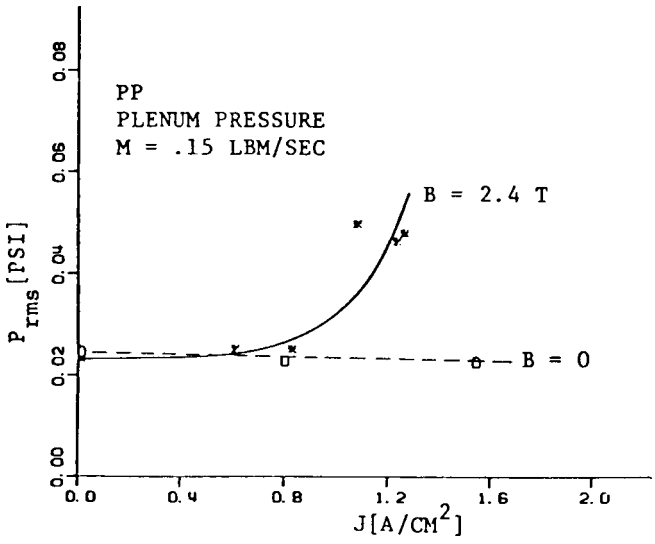


Fig. 2a. Plenum pressure fluctuation level, M = .15 LBM/SEC.

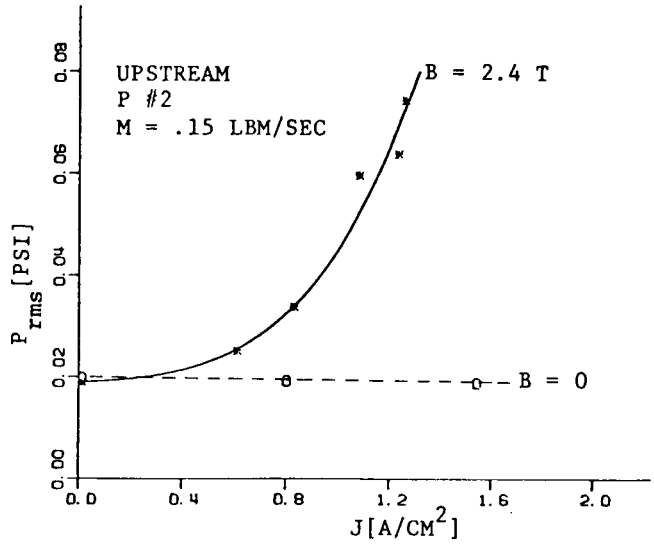


Fig. 2b. Upstream pressure fluctuation level, M = .15 LBM/SEC.

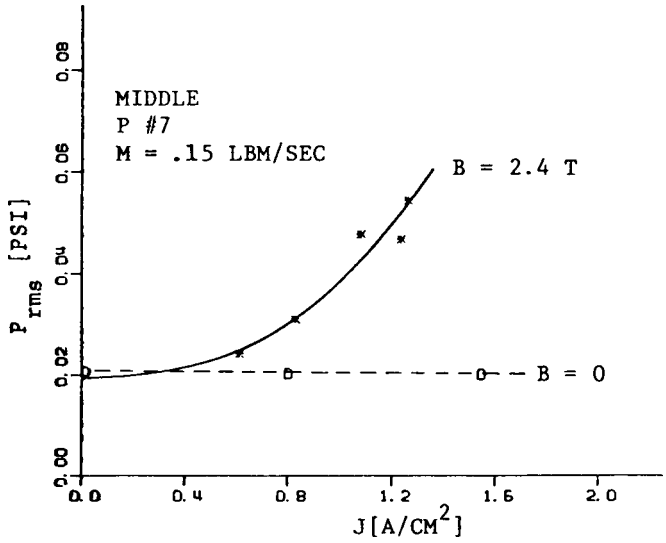


Fig. 2c. Middle pressure fluctuation level, M = .15 LBM/SEC.

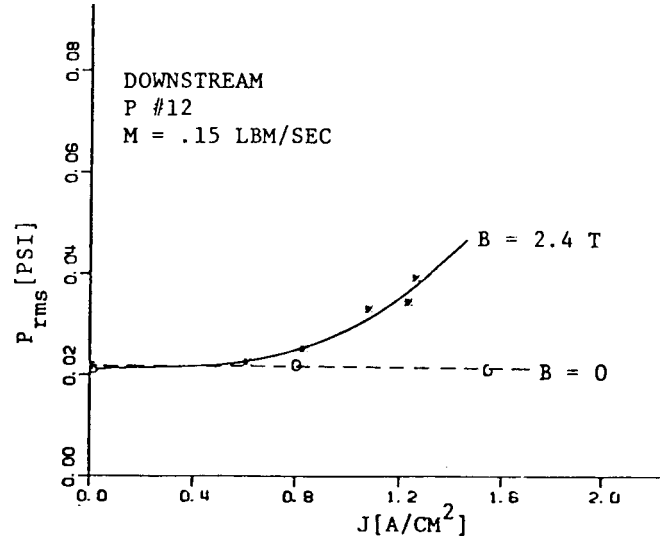


Fig. 2d. Downstream pressure fluctuation level, M = .15 LBM/SEC.

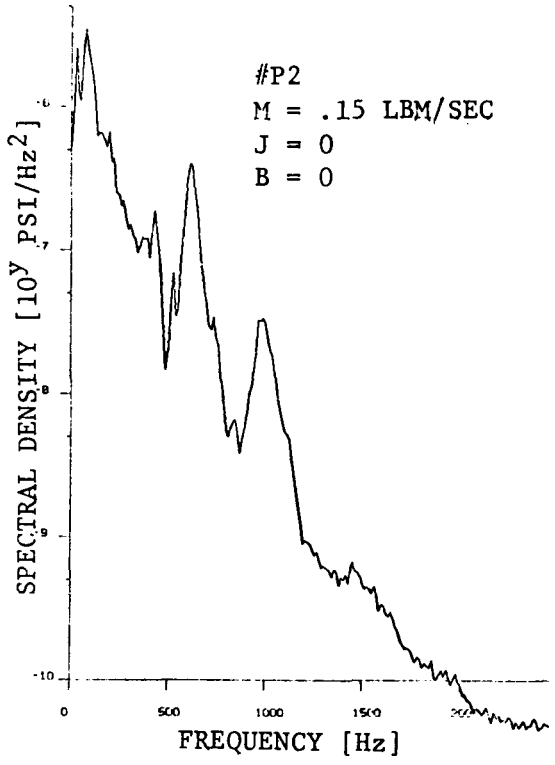


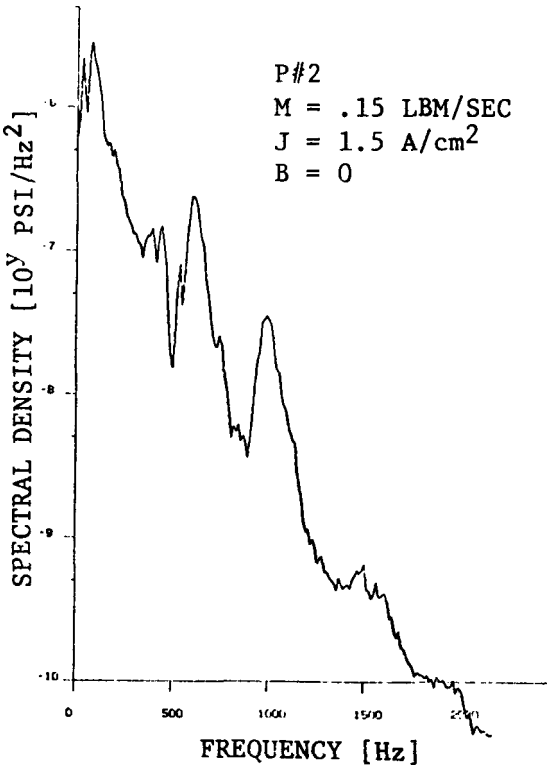


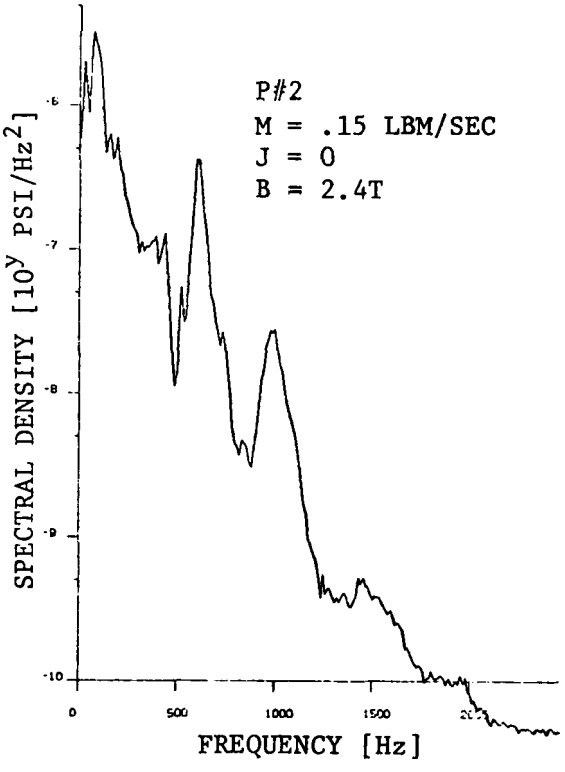


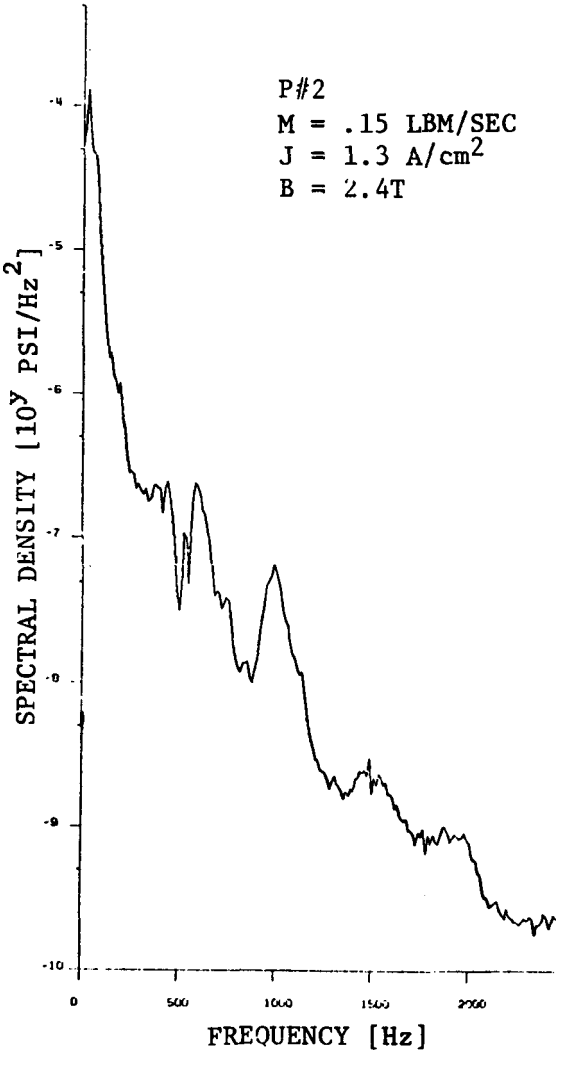


Fig. 3. Frequency spectra of upstream pressure fluctuations as a function of current and magnetic field. Faraday generator configuration

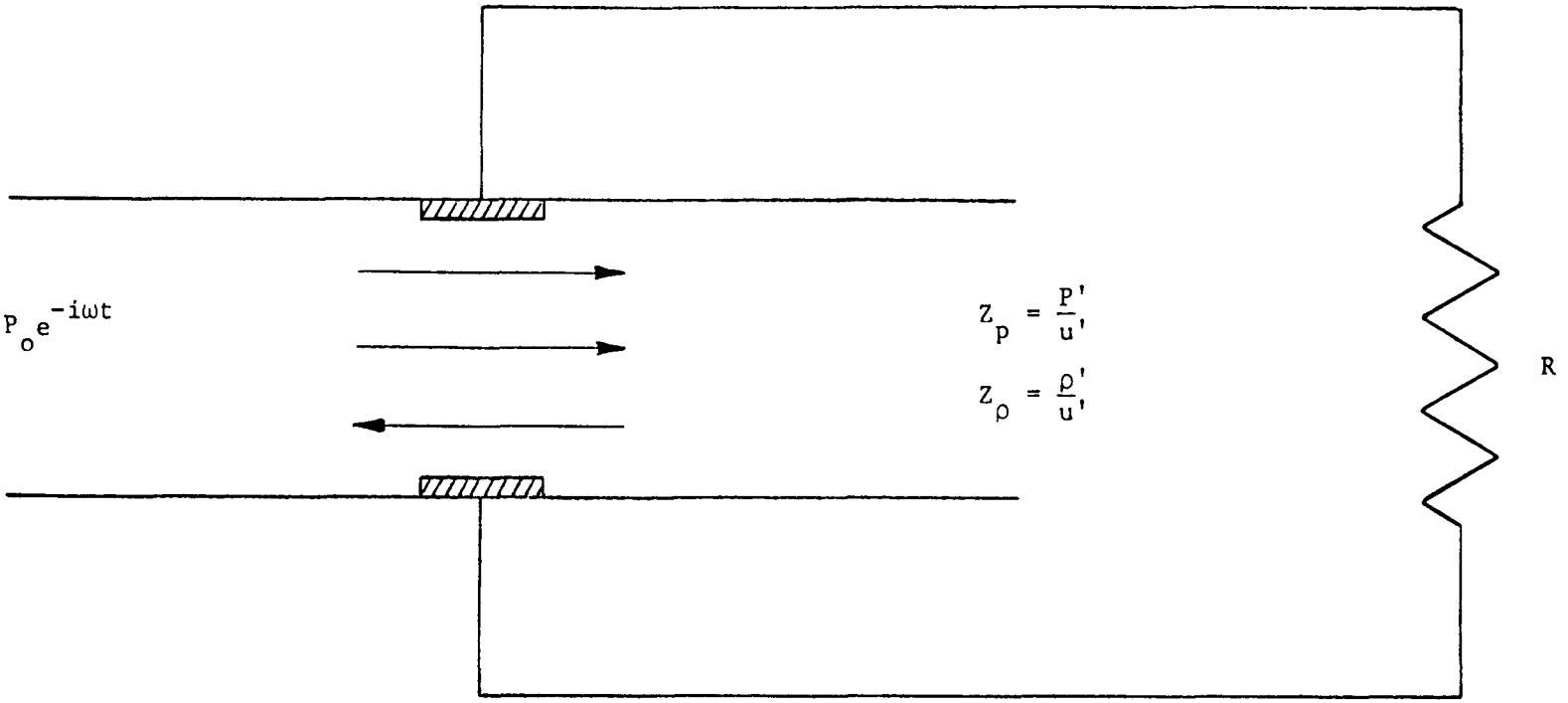


Fig. 4. The boundary value problem for a Faraday generator.

Of particular interest in interpreting the results of the theory is the average fluctuation energy flux necessary to sustain a unit pressure fluctuation level at the entrance of the generator (i.e., as produced by the combustor). A positive value of average fluctuation energy flux at the inlet indicates the generator acts as a passive element, absorbing energy from the combustor. A negative value at the inlet indicates the generator acts as an active element, feeding energy back into the combustor, and corresponds to an unstable condition.

The results of this type of analysis using parameters which correspond to the low velocity conditions of the M-2 experiment are shown in Figure 5. The theory is in good agreement with experimental observations. There is negligible effect of either current or magnetic field alone in comparison with the baseline no current, no magnetic field case. The combination of both current and magnetic field, as in normal generator operation, shows a negative average fluctuation energy flux and an unstable situation in the low frequency range. The cutoff frequency for negative energy flux is approximately 70 Hz, which corresponds well with the experimental observation of low frequency growth.

Results of the preceeding boundary value problem approach as calculated for values of the parameters representative of a central station near-sonic Faraday generator are shown in Figure 6. The stable and unstable regions are plotted versus the load factor, $K_F$, and the interaction parameter, S. (The interaction parameter here is defined as the ratio of the length of the generator to the interaction length, $S = L/L_i = \sigma B^2 L/\rho u$. Large scale generators may have values of S as large as ten.) It is seen that the theory predicts an unstable operating regime near short circuit (small load factor), but for more normal loading ($K_F$ = .5 - .8) the theory predicts stable operation.

Comparison of other aspects of the theory with experimental results obtained in the last test are being analyzed. In addition, the boundary value stability analysis, as it applies to a diagonal wall generator is being developed. A future experiment is planned in which theoretical predictions of the new theory will be subjected to more detailed scrutiny.

### 3.1.2 Plasma Nonuniformity Studies

Recent work has focused on the development of a laser fluorescence diagnostic. The purpose of this diagnostic is to measure temperature and electrical conductivity fluctuations in an MHD channel. The technique uses a cw dye laser to pump a transition between two excited levels of sodium which is seeded in the combustion gases. An enhanced spontaneous emission signal from the upper level (fluorescence) is observed along a line of sight perpendicular to the exciting laser beam. This signal can thus be spatially resolved to the small volume intersected by the laser beam and the collection line of sight.

The interpretation of the signal is based upon a rate-equation description of the sodium level populations. The levels of interest are the 3P

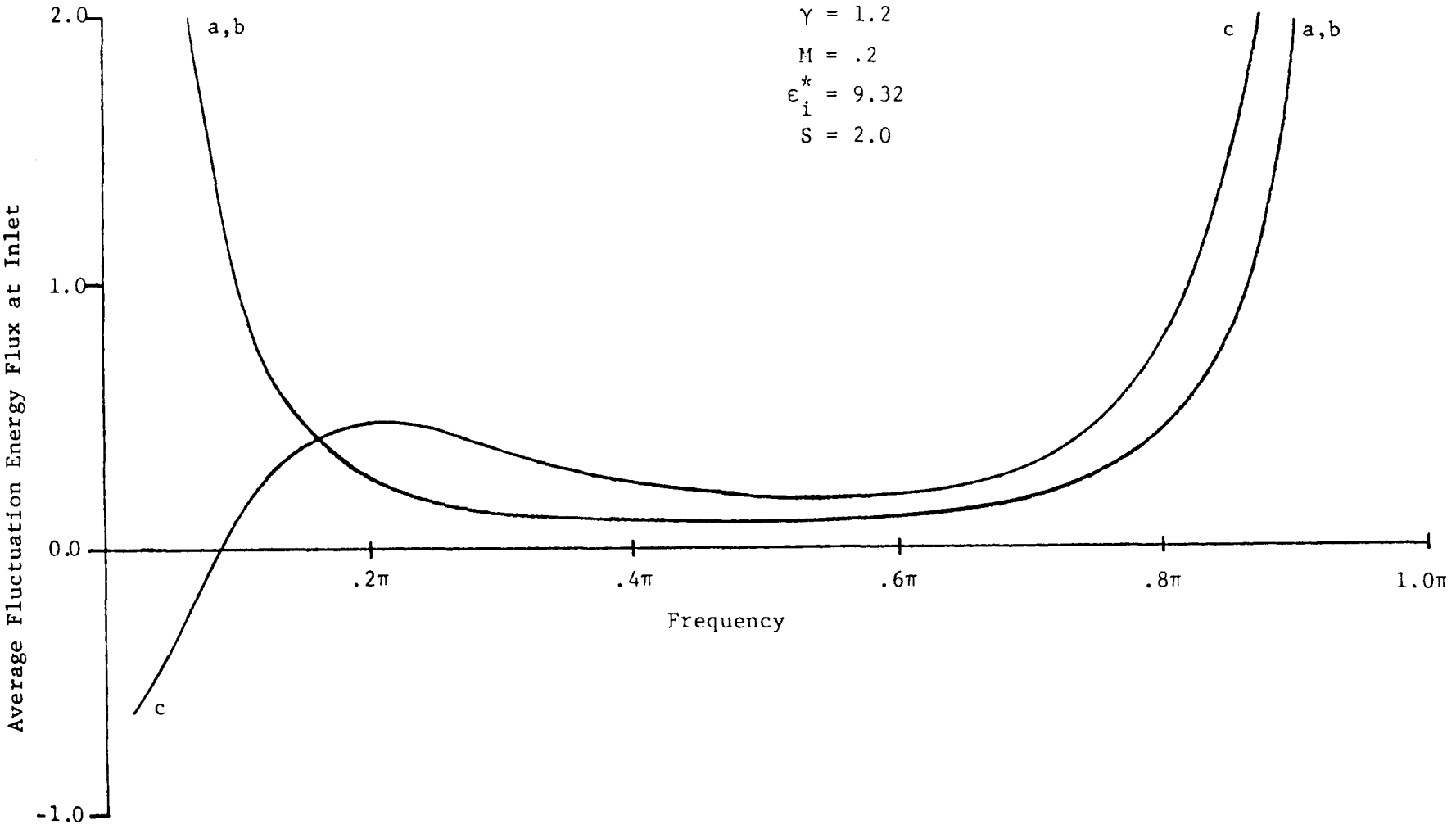


Fig. 5. Dimensionless average fluctuation of energy flux at the inlet of a Faraday generator to sustain a constant inlet pressure fluctuation level as a function of frequency. (a) case of J = 0, B = 0 and the case of J = 0, B ≠ 0. (b) the case of J ≠ 0, B = 0. (c) the case of J ≠ 0, B ≠ 0.

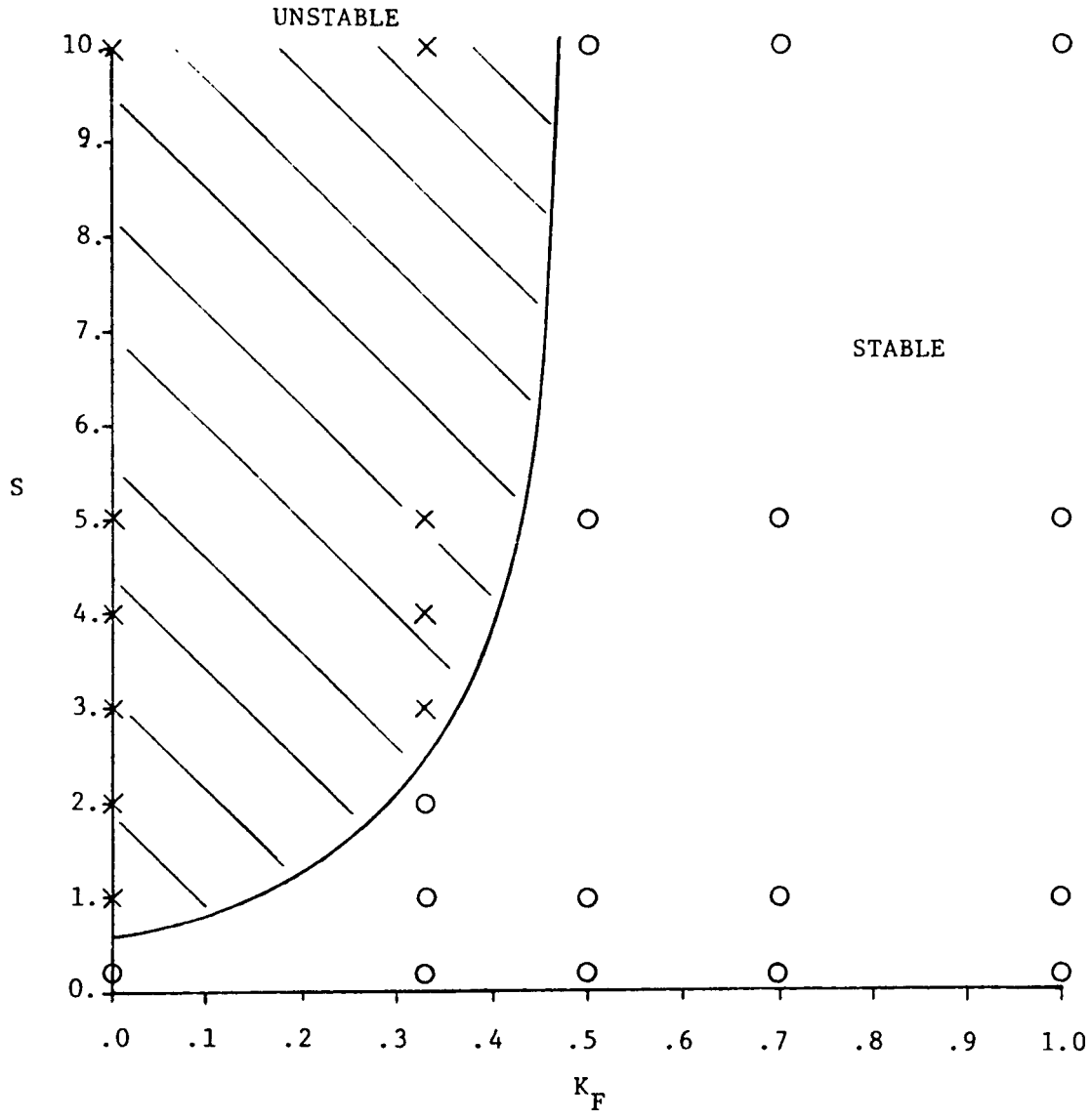


$\gamma = 1.2$

$M = .8$

$\varepsilon_i^* = 10.07$

Fig. 6. Stability plot for Faraday generator versus interaction parameter and the load parameter.

and 4D. Transitions between the two doublets occur at 5682 Å and 5688 Å (Figure 7). A simplified equation governing the steady-state population of the 4D level is

$$\frac{d\, n_2}{dt} = 0 = n_1 W_{12} - n_2 \nu_q$$

where the n's are number densities of the indicated states, $W_{12}$ is a laser intensity dependent transition probability, and $\nu_q$ is a collisional quenching frequency. It has been assumed that laser absorption and collisional quenching are the dominant processes. Since $n_2$ is about $10^{-4}\, n_1$ for thermal equilibrium at combustion temperatures, one can select a laser intensity which increases $n_2$ significantly but leaves $n_1$ relatively undisturbed. Then, assuming $n_1$ to be in thermal equilibrium with the ground state, one finds

$$n_2 = \frac{3\, n_o \exp(-h\nu_{01}/kT)\ (W_{12})}{\nu_q}$$

where h is Planck's constant, k is Blotzmann's constant, T is the gas temperature and $\nu_{01}$ is the frequency corresponding to the energy difference between the ground and first excited level.

The fluorescence signal at 5682 Å or 5688 Å in an optically thin gas is linearly proportional to $n_2$; therefore, the fluorescence signal can be a sensitive indicator of the gas temperature through the exponential factor $\exp(-h\nu_{01}/kT)$. Since electrical conductivity is a strong function of temperature, the signal should also be a reasonable indicator of the electrical conductivity of the gas. Many of the quantities involved in $\nu_q$ and $W_{12}$ have large uncertainties which make absolute temperature and conductivity measurements difficult; however, with proper calibration the fluorescence technique should provide useful information on temperature and conductivity fluctuations.

A check out experiment with a Perkin-Elmer air-acetylene burner and a Spectra-Physics cw dye laser has been set up. A schematic of the apparatus is shown in Figure 8. Steady-state spectra of the 3P - 4D transitions have been measured with up to 200 mW of laser power at either 5682 Å or 5688 Å. Results from these measurements were as follows:

1. Fluorescence signals were easily detectable.

2. The ratios of fluorescence signals at 5688 Å to those at 5682 Å did not equal the ratio anticipated for thermal equilibrium within the 4D level. The fluorescence signal at the laser wavelength was was always larger than the signal predicted by the magnitude of the other fluorescence signal.

3. A scatter signal at the laser wavelength was observed in the spectra when the laser was detuned from the resonant lines.

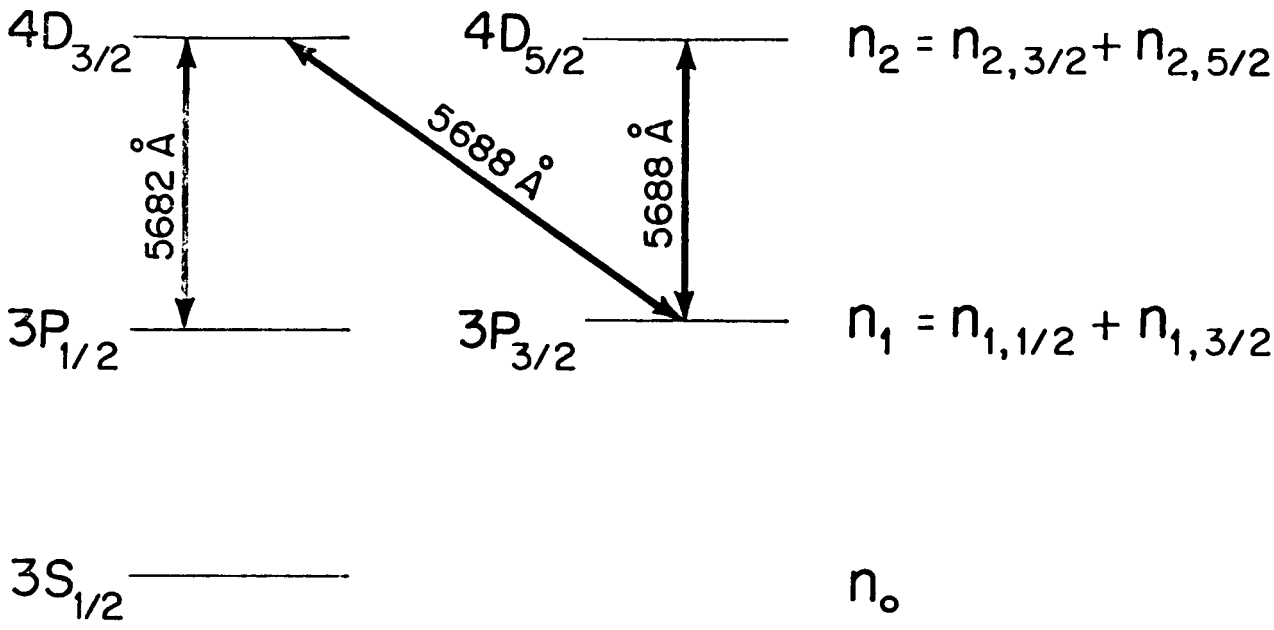


Fig. 7. Sodium Energy Level Diagram

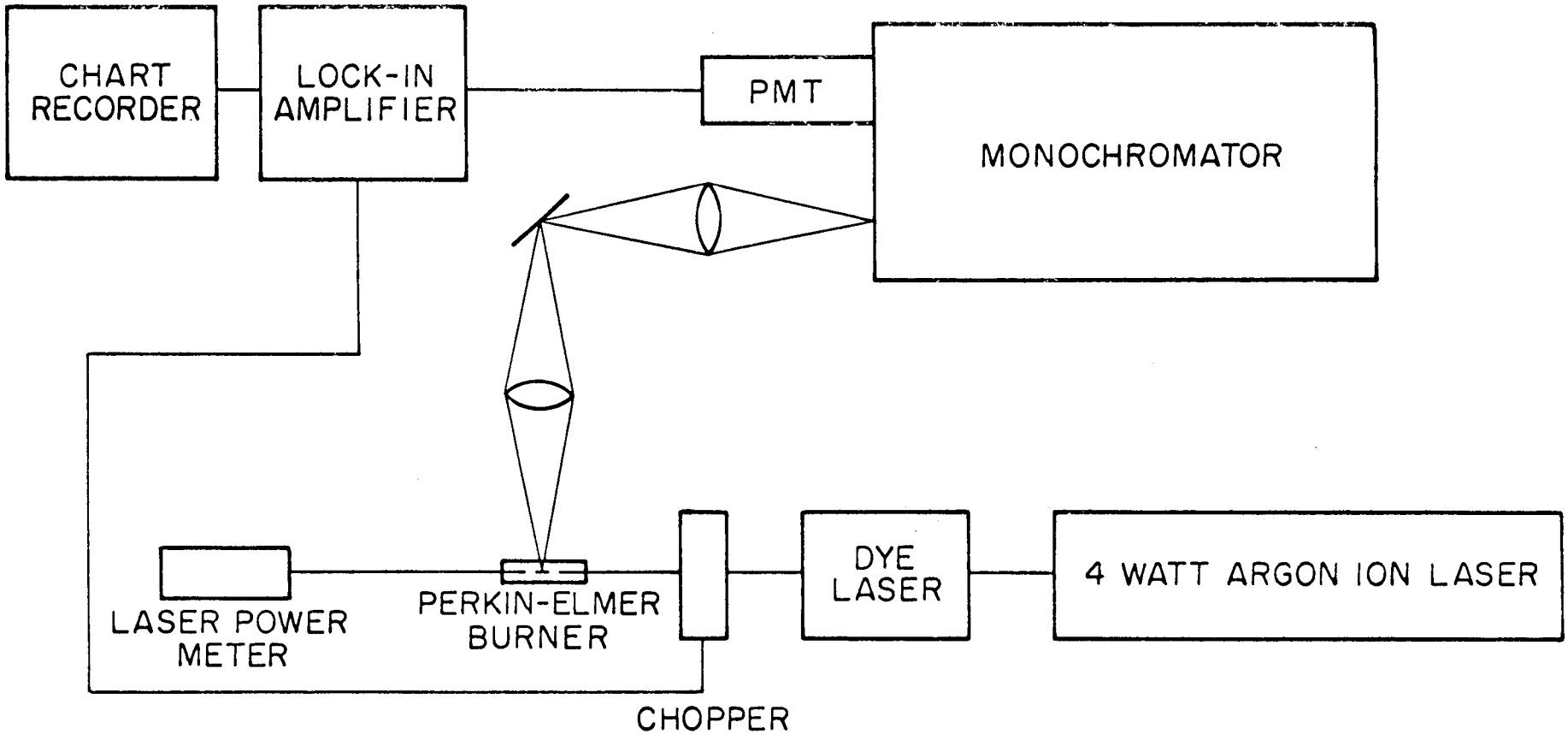


Fig. 8. Laser Fluorescence Experimental Apparatus

4. After a scatter component was subtracted from the laser wavelength fluorescence signal, the ratio of the fluorescence signals still deviated from the thermal equilibrium value with the signal at the exciting wavelength too large.

A possible explanation of the signal ratios involves the collisional mixing of the two states within the 4D doublet. One can write a new set of rate equations which include the effects of doublet mixing. Considering laser excitation at 5688 Å the rate equations are

$$\frac{d\, n_{2,5/2}}{dt} = 0 = n_{1,3/2}\, W_{1,3/2;2,5/2} + n_{2,3/2}\, \nu_{3/2,5/2} - n_{2,5/2}\, \nu_{5/2,3/2} - n_{2/5/2}\, \nu_q$$

and

$$\frac{d\, n_{2,3/2}}{dt} = 0 = n_{1,3/2}\, W_{1,3/2;2,3/2} + n_{2,5/2}\, \nu_{5/2,3/2} - n_{2,3/2}\, \nu_{3/2,5/2} - n_{2/3/2}\, \nu_q$$

Here $\nu_{3/2,5/2}$ and $\nu_{5/2,3/2}$ are the collisional mixing frequencies, and we assume that they satisfy the thermal equilibrium ratio

$$\frac{\nu_{3/2,5/2}}{\nu_{5/2,3/2}} = 1.5$$

We also assume that the transition probabilities are in the same ratio as their respective oscillator strengths

$$\frac{W_{1,3/2;2,3/2}}{W_{1,3/2;2,5/2}} = \frac{1}{9}$$

Incorporating these two assumptions in the rate equations one finds

$$\left.\frac{n_{2,5/2}}{n_{2/3/2}}\right|_{\substack{5688\ \text{Å} \\ \text{excitation}}} = \frac{10 + 9\left(\dfrac{\nu_q}{\nu_{3/2,5/2}}\right)}{\dfrac{20}{3} + \dfrac{\nu_q}{\nu_{3/2,5/2}}}$$

A similar expression can be derived for 5682 Å excitation, namely,

$$\left.\frac{n_{2,5/2}}{n_{2/3/2}}\right|_{\substack{5682\ \text{Å} \\ \text{excitation}}} = \frac{1}{\frac{2}{3} + \frac{\nu_q}{\nu_{3/2,5/2}}}$$

In an optically thin gas, the fluorescence signals are proportional to the product of state number densities and their respective Einstein A Coefficients. Thus, for the 3P-4D doublet the ratio of fluorescence signals at 5688 Å to signals at 5682 Å will be

$$FR = \frac{A_{2,5/2;1,3/2}\ n_{2,5/2} + A_{2,3/2;1,3/2}\ n_{2,3/2}}{A_{2,3/2;1,1/2}\ n_{2,3/2}}$$

Since

$$\frac{A_{2,3/2;1,1/2}}{A_{2,5/2;1,3/2}} = \frac{5}{6}$$

and

$$\frac{A_{2,3/2;1,3/2}}{A_{2,5/2;1,3/2}} = \frac{1}{6}$$

the fluorescence ratio becomes

$$FR = \frac{\frac{n_{2,5/2}}{n_{2,3/2}} + \frac{1}{6}}{\frac{5}{6}}$$

This expression together with the relations for the population ratio $n_{2,5/2}/n_{2,3/2}$ can be used to explain the observed fluorescence ratios. Experimental fluorescence ratios from 5682 Å excitation were used to calculate

$$n_{2,5/2}/n_{2,3/2}\ _{5682\ \text{Å excitation}}$$

This value was subsequently used to calculate $(\nu_q/\nu_{3/2,5/2})$ which in turn was used to predict

$$n_{2,5/2}/n_{2,3/2}\ _{5688\ \text{Å excitation}}$$

and the corresponding fluorescence ratio. This predicted ratio agreed with the experimental results to better than 95%. The calculated value of

($\nu_q/\nu_{3/2,5/2}$) was approximately 0.7; however, no experimental data are available for direct comparison. Data from Lijnse and Hornman [1] show that quenching cross sections can be of the same order of magnitude as mixing cross sections for the 4P level of potassium. One might expect that quenching cross sections would increase more than mixing cross sections for higher lying levels. The presence of lower states with slightly different energies could significantly augment collisional quenching, but it might not affect doublet mixing. Thus, the value of ($\nu_q/\nu_{3/2,5/2}$) = 0.7 does not appear unreasonable for the 4D level of sodium.

The effects of doublet mixing do not alter the application of the diagnostic to conductivity fluctuation measurements. It is still likely that the temperature sensitivity of the exponential factor will dominate the fluorescence signal. Future work will involve a comparison of laser fluorescence and line-reversal temperature measurements including both steady state and controlled fluctuation cases.

## 3.2 Work Area II - Boundary Layer and Hall Field Phenomena

### 3.2.1 Insulating Wall Boundary Layer

Measurements of the insulating wall velocity profiles using laser anemometry have previously been reported. These profiles were obtained for three separate generator conditions. The first profile was obtain without either a magnetic field or a current. The second profile was obtained with a magnetic field of 2.4 Tesla and no net current. The third profile was obtained with both a magnetic field of 2.4 Tesla and an average current density of 0.74 amp/cm$^2$. These measured velocity profiles are shown again in Figures 9 -11 for convenience.

Further analysis of the laser anemometry data has yielded turbulence intensity profiles for the three generator conditions. The turbulence intensity is the root-mean-square of the velocity fluctuations normalized by the centerline velocity, and is an important measure of the turbulence. The turbulence intensity profiles for the three generator cases are presented in Figures 12-14. The increase in turbulence intensity toward the wall is expected boundary layer behavior. The high, 5-6 percent turbulence intensity near the center of the channel is in agreement with previous measurements of the outlet conditions of the M-2 burner and with electrode wall measurements of Daily [2].

Figure 15 shows the ratio of the turbulence intensity with magnetic field, both with and without net current, to the turbulence intensity without magnetic field. The accuracy of the ratio or "damping factor" data does not warrant interpretation of the trends of the damping factor as a function of position in the boundary layer. The data, however, clearly indicate that turbulence damping was present with an average value of approximately 0.8. Olin [3] made measurements to determine the turbulence damping in a combustion plasma with flow conditions similar to the present measurements. Olin's results would predict a damping factor of 0.94 for the present conditions of a Reynolds number of 8200 and a Hartmann number of 24 based on the channel half width. Although

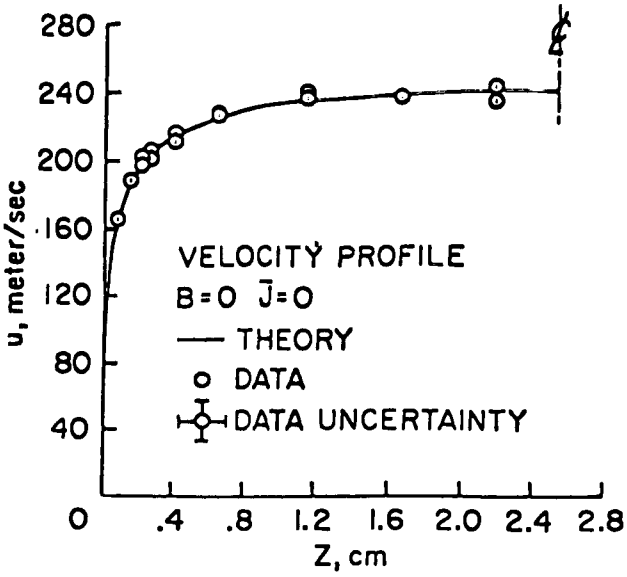


Figure 9. Control Sidewall Profile

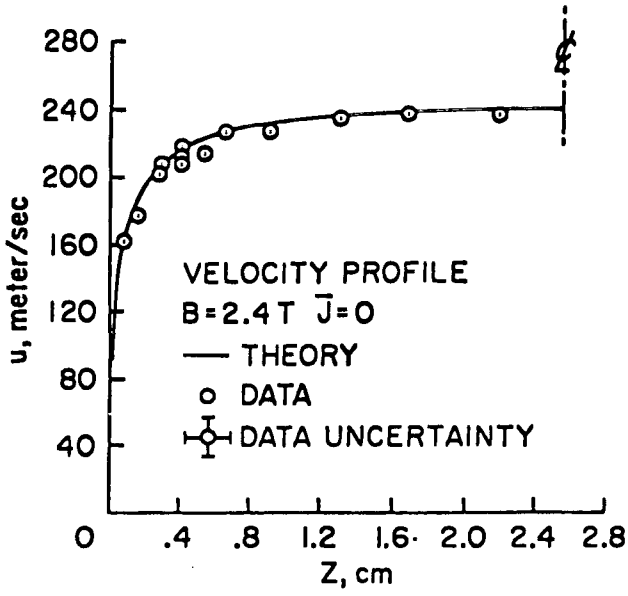


Figure 10. Hartmann Sidewall Profile with Zero Average Current Density.

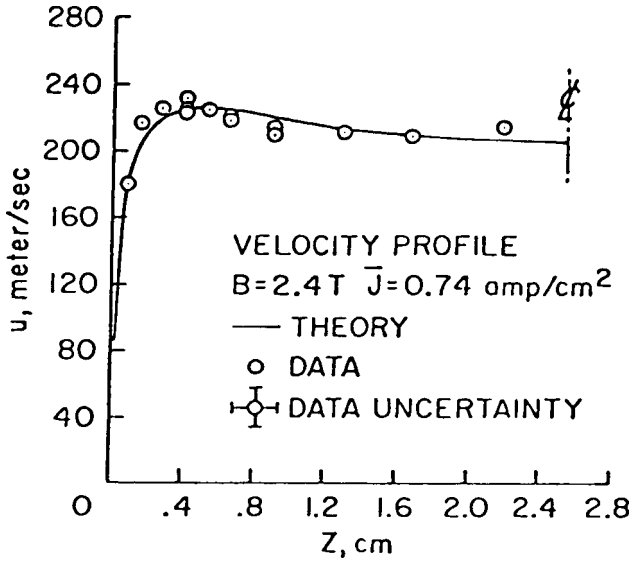


Figure 11. Hartmann Sidewall Profile with Current and Magnetic Field.

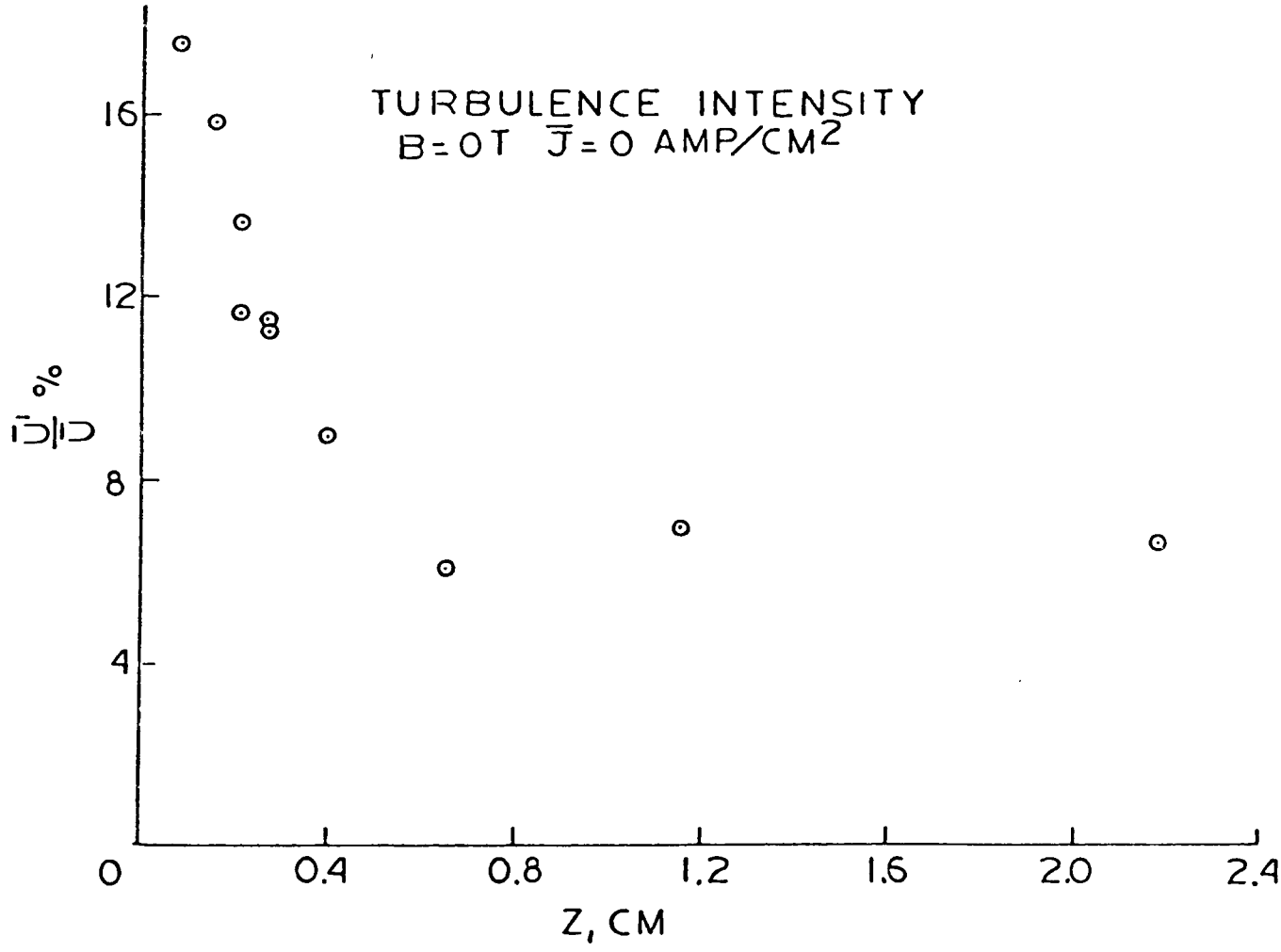


Figure 12. Control Sidewall Turbulence Intensity.

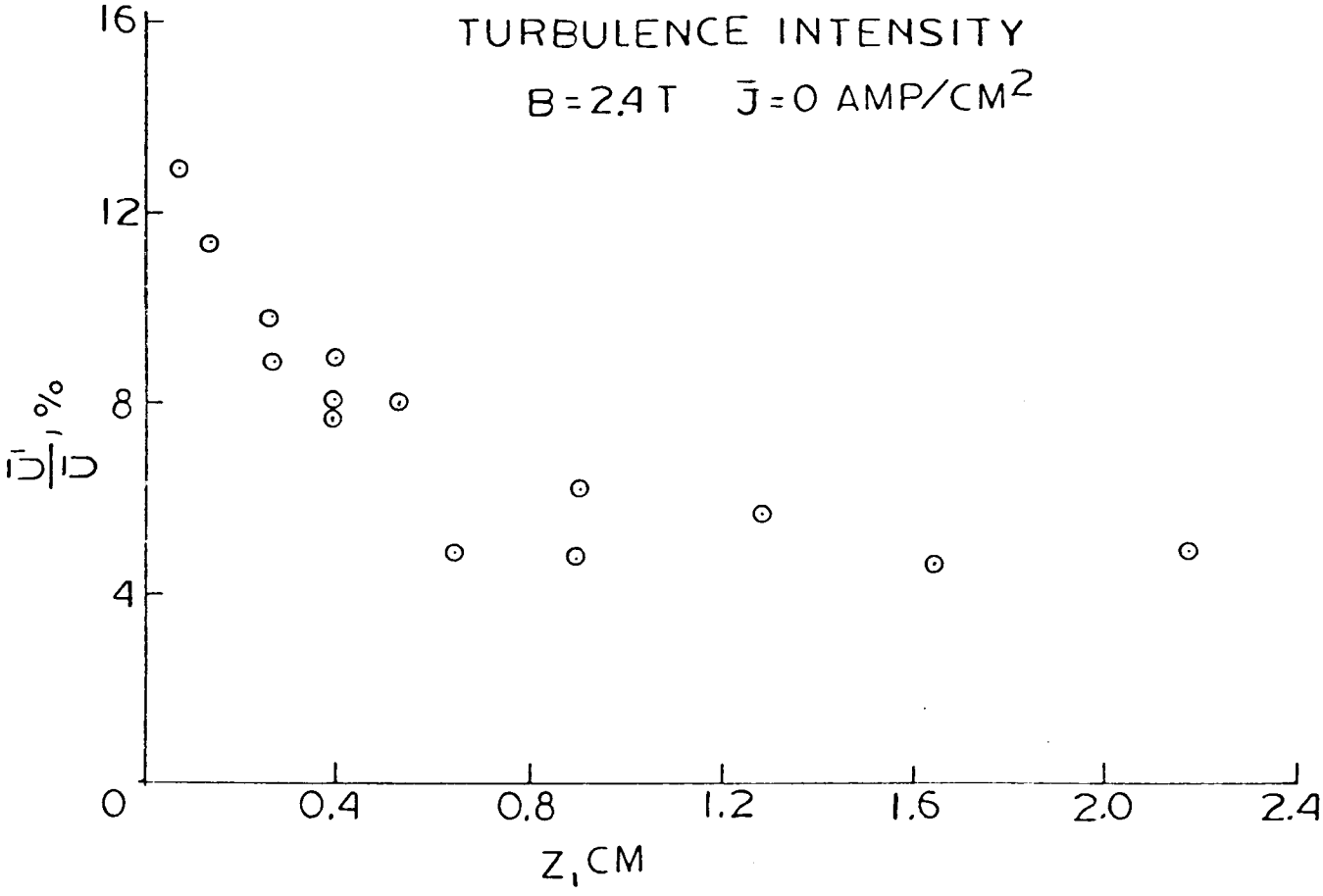


Figure 13. Sidewall Turbulence Intensity with Zero Average Current.

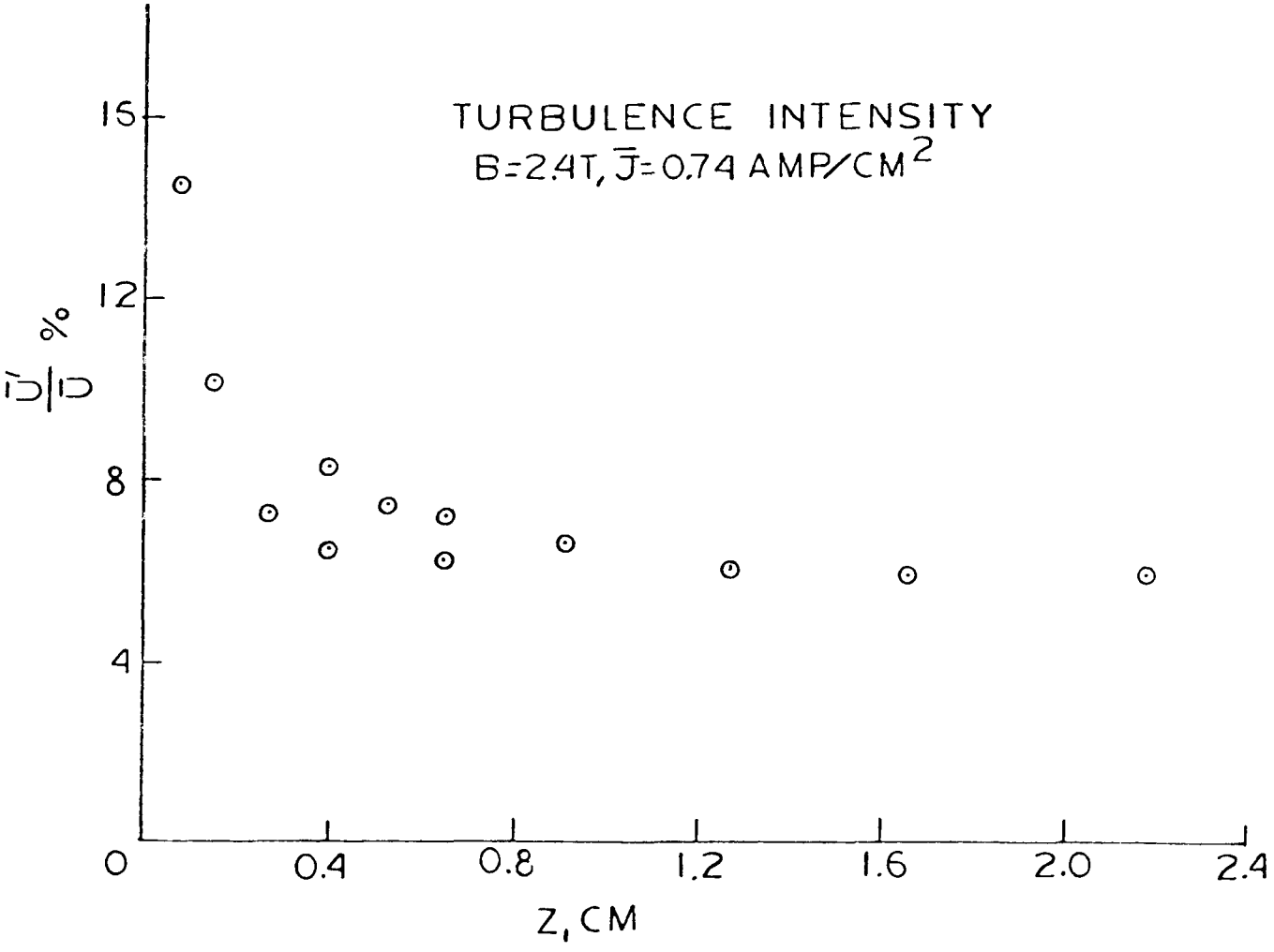


Figure 14. Sidewall Turbulence Intensity with Current and Magnetic Field.

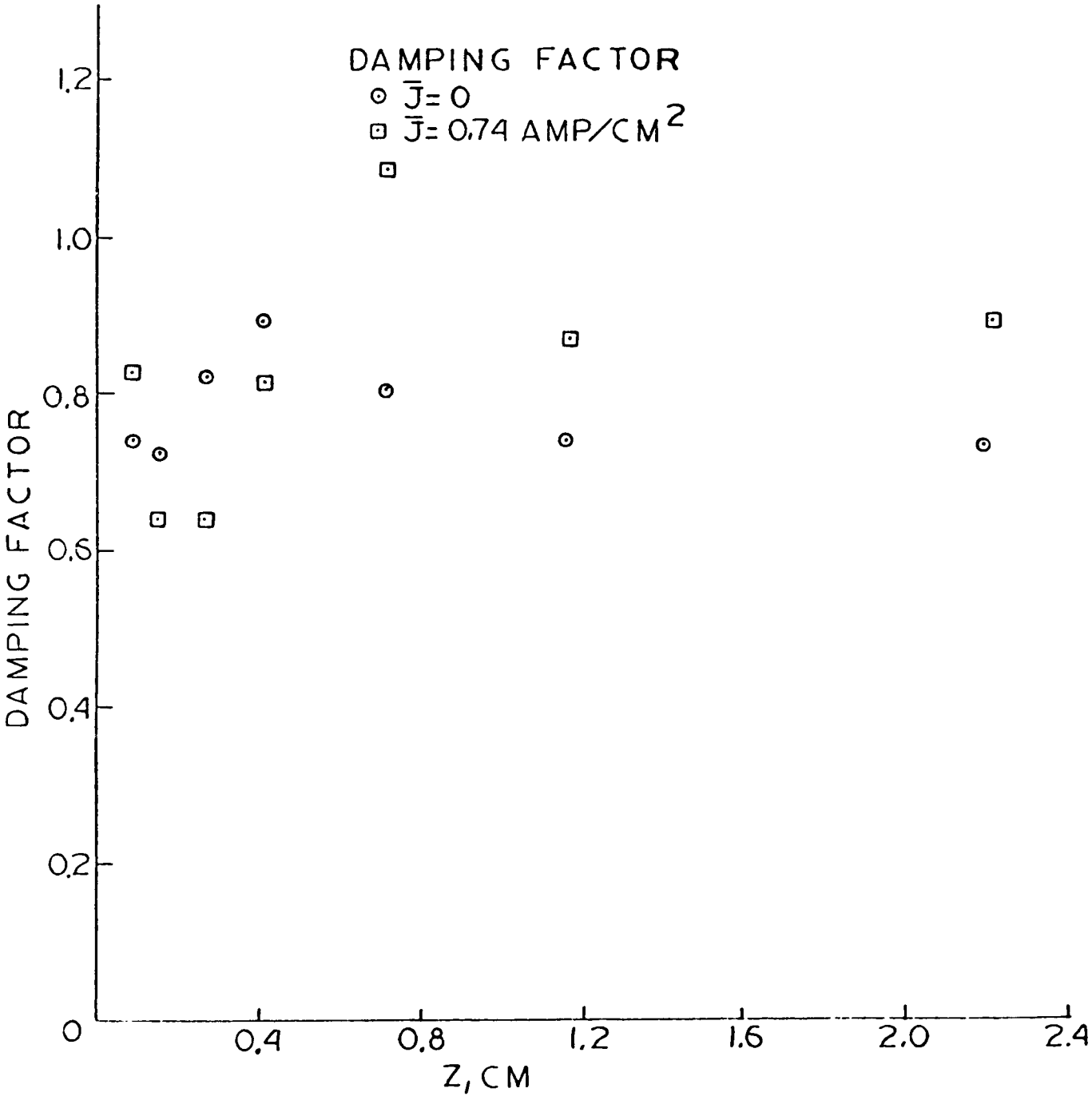


Figure 15. Sidewall Turbulence Damping Ratio for 2.4 Tesla Magnetic Field.

turbulence damping has no significant effect on the present profiles, according to the theory developed by Olin, turbulence damping is a function of the square of the Hartmann number divided by the Reynolds number. This ratio is proportional to the length scale and the square of the magnetic field and is inversly proportional to the velocity. Thus the effects of turbulence damping are expected to increase substantially for central station MHD power generation plants as compared to the present experiments due to both the increased size and magnetic field strength of such generators.

Calculations have been made to determine the importance of extended Hartmann flow and turbulence damping in an ETF size generator. The assumed generator has a thermal input of 250 megawatts, a 6 Tesla magnet and a constant 800 m/sec velocity down the duct. The electrical output of the channel was computed using a one-dimensional program which includes electrical boundary layer losses. A summary of this computation is presented in Table 2. In this table P and T are the static pressure and temperature while $E_x$ is the Hall field. $V_{out}$ is the terminal voltage of the generator while $V_{loss}$ is the voltage drop in the boundary layers. $J_y$, the average current density in the generator, was used as input into the insulating wall boundary layer code.

Four separate boundary layer calculations were made. The first two calculations were made allowing the current density to vary according to the insulating wall electrical model. These calculations were made with and without turbulence damping. The second two cases provide a reference and are calculations with a constant current density across the boundary layer. Again these calculations were made with and without turbulence damping.

The skin friction coefficient for these four calculations is presented in Figure 16. The effect of turbulence damping for both the varying current, extended Hartmann case and the uniform current case is to reduce the skin friction by 25%. The effect of extended Hartmann flow is seen to increase the skin friction by 120% as compared to the uniform current case. Thus it can be concluded that both extended Harmann flow and turbulence damping will be significant in the ETF generator.

The Stanton number, or heat transfer coefficient, is presented in Figure 17. The effect of extended Hartmann flow on the heat transfer is seen to be much more moderate than the skin friction with a 25% increase in heat transfer while at the same time turbulence damping reduces the heat transfer by 25%.

These calculations indicate that in the design of the ETF generator it is important to consider both the effects of extended Hartmann flow and turbulence damping.

### 3.2.2 Electrode Wall Boundary Layer

A series of runs was performed to measure temperatures and electron number densities in an electrode wall boundary layer. The purpose of the experiments was to observe electron non-equilibrium in the inner regions of the boundary layer, and to measure the effects of Joulean heating on the temperature and electron number density profiles. The hardware for the run consisted of the Stanford M-2 facility burner, plenum, run-in section, and generator. The

Table 2. ETF Generator Electrical Conditions

B = 6 Tesla T = 800 m/sec Height = 0.5 m T(electrode) = 1300 K

| X m | P atm | T K | Area $m^2$ | $E_x$ KV/m | $V_{out}$ Volt | $V_{loss}$ Volt | $J_y$ $A/cm^2$ | $P_{out}$ $M_w$ |
|---|---|---|---|---|---|---|---|---|
| 0.20 | 5.00 | 2835 | 0.079 | - | - | - | - | 0.9 |
| 0.46 | 4.73 | 2821 | 0.084 | 0.90 | 1673 | 135 | 1.59 | 1.2 |
| 0.98 | 4.24 | 2793 | 0.093 | 0.96 | 1667 | 164 | 1.39 | 3.4 |
| 2.02 | 3.37 | 2737 | 0.116 | 1.08 | 1656 | 218 | 1.08 | 7.8 |
| 3.06 | 2.67 | 2681 | 0.145 | 1.19 | 1646 | 272 | 0.84 | 12.1 |
| 4.10 | 2.11 | 2625 | 0.180 | 1.28 | 1635 | 331 | 0.63 | 16.1 |
| 5.14 | 1.68 | 2570 | 0.221 | 1.31 | 1624 | 391 | 0.46 | 19.7 |
| 6.18 | 1.37 | 2519 | 0.267 | 1.30 | 1613 | 448 | 0.32 | 22.9 |
| 7.22 | 1.14 | 2473 | 0.316 | 1.24 | 1602 | 496 | 0.22 | 25.5 |
| 8.26 | 0.97 | 2431 | 0.366 | 1.17 | 1590 | 532 | 0.15 | 27.5 |
| 9.30 | 0.84 | 2395 | 0.415 | 1.11 | 1579 | 557 | 0.10 | 29.1 |
| 9.82 | 0.80 | 2378 | 0.439 | 1.09 | 1574 | 567 | 0.09 | 29.8 |

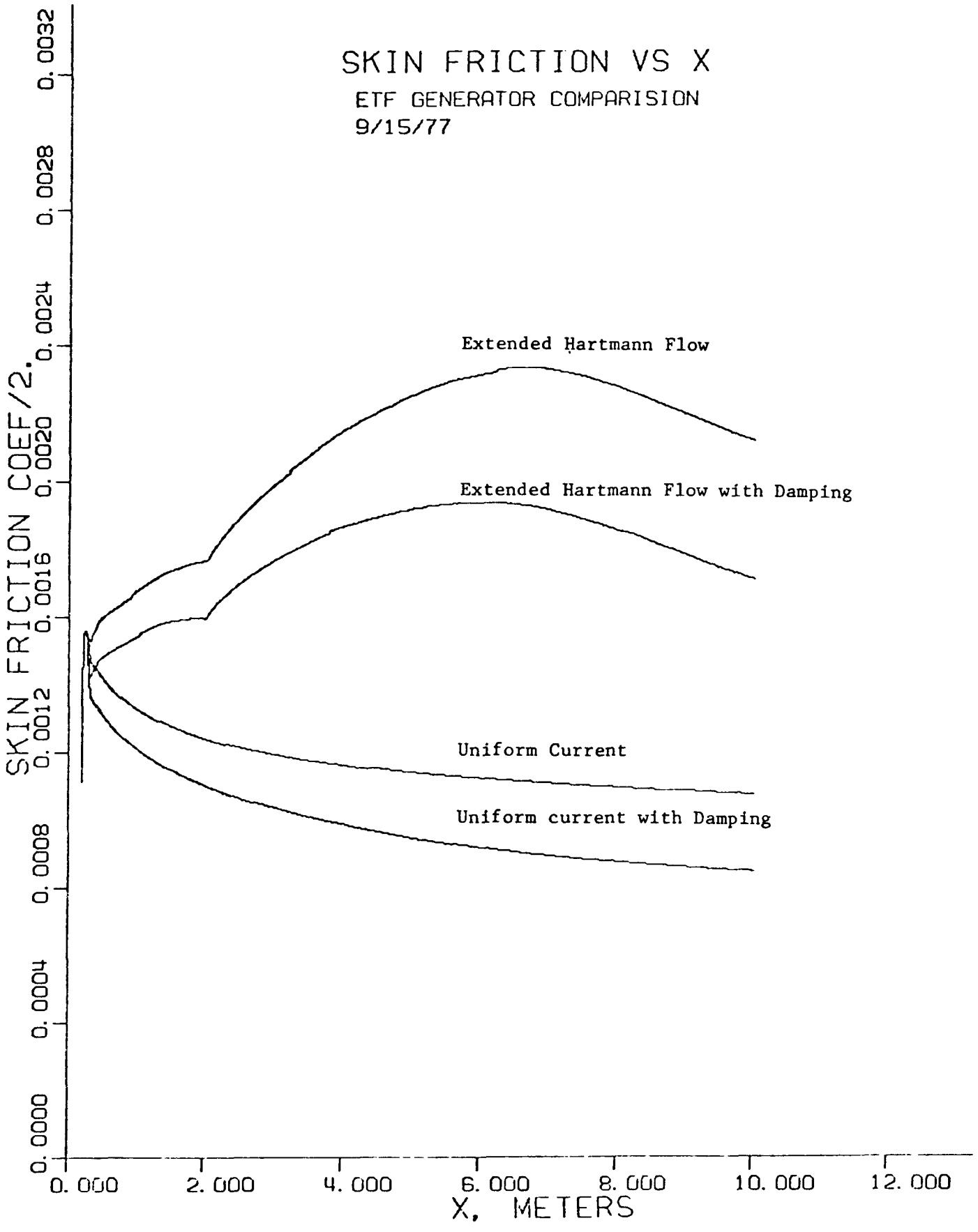


Figure 16. ETF Generator Predictions of Skin Friction Coefficient

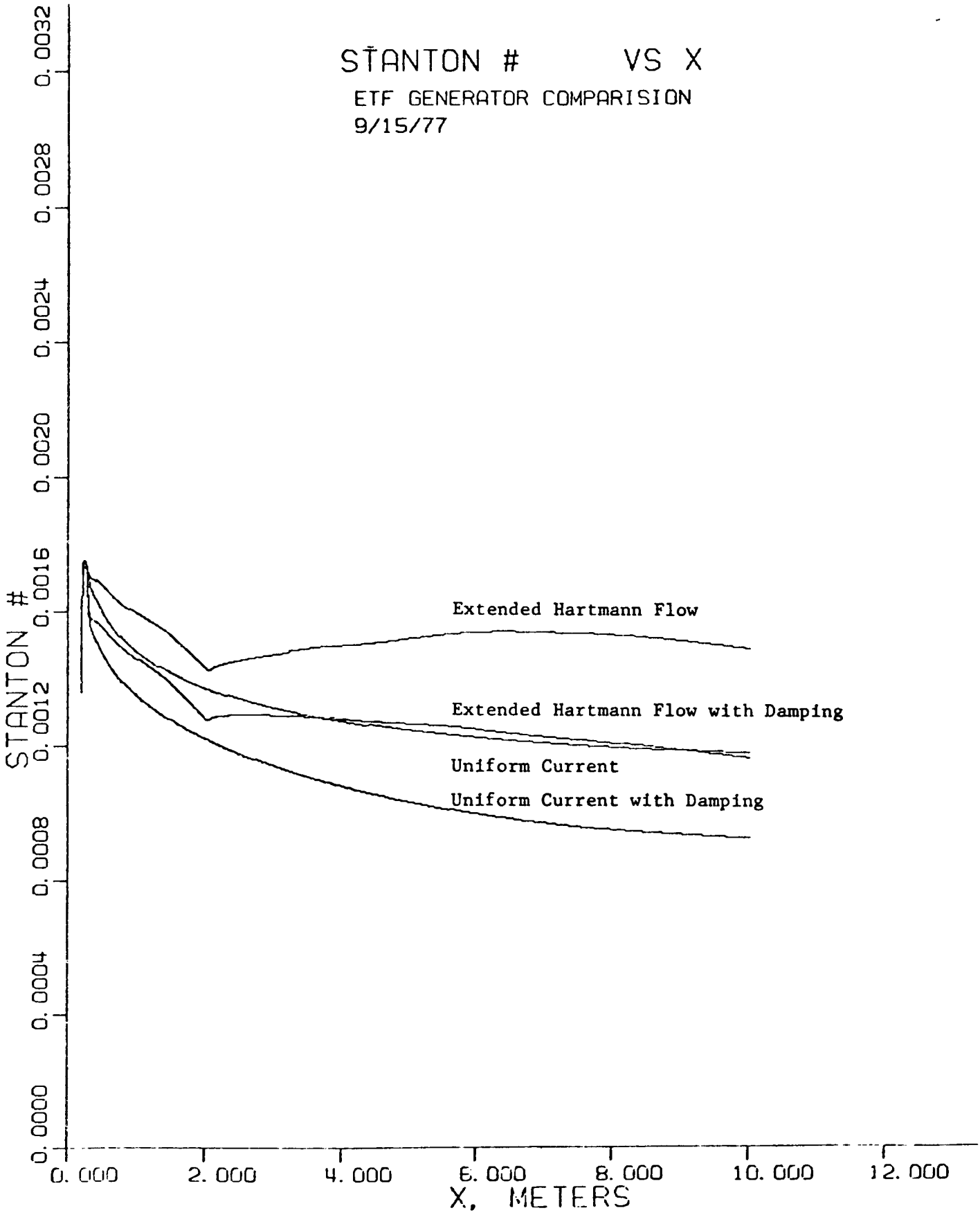


Figure 17. ETF Generator Predictions of Heat Transfer Coefficient

generator had thirteen electrode pairs, with battery banks used to supply an electric field. No magnetic field was used in the experiment. Diagnostics for the experiment included optical temperature and electron number density measurements in the boundary layer, and voltage pins along the side wall to measure electrode voltage drops.

The experiments were run over a period of three test days. On the first day, the electrodes were running too cold, and seed deposits on the electrode prevented any usable data from being taken. On the second and third run days, the electrodes were operated hotter by adjusting the flow conditions, and the seed deposition problem was virtually eliminated. Seed still collected slowly along the edges of the electrode being viewed by the optical diagnostics, and as this seed obscured the view of the last millimeter of the boundary layer, it had to be scraped off periodically during the run. With this procedure successful, measurements were made during these two days of temperature and electron number density profiles in the boundary layer at two flow conditions, and a variety of current settings.

Although the data for the experiment are still being reduced, some preliminary results will be presented here. Figure 18 shows data for temperature profiles in the channel with and without current. This run was performed with a free stream velocity of around 300 meters per second, a pressure of one atmosphere, and a nitrogen to oxygen mass ratio of one half. The run with current had an average current density of 1.5 amps/$cm^2$ over .46 meters length, with a total of 56.3 kilowatts being dissipated in the channel. The temperature profile with current is seen to be considerably steeper near the wall than the profile without current. This will cause substantial changes in wall heat transfer and boundary layer voltage drops.

At the present time, the optical diagnostic data are being reduced and corrected for boundary layer effects. Upon completion of the data reduction, the profiles will be compared to predictions from a boundary layer computer program in order to test the ability of theory to predict temperature and electron number density profiles with and without current.

## 3.3 Work Area III - Six Tesla Magnet Investigations

### 3.3.1 Disk Generator Program

Efforts were directed toward the construction of the six tesla disk generator experimental facility and toward the analytical studies to predict the performance of the present disk generator facility and to assess the applicability of the disk generator to the commercial MHD power plant.

The main components of the disk generator experimental facility underwent a series of thermal tests for a total operation time of 4 hours. The disk generator insulator plates constructed with metalyzed $M_gO$ ceramics were tested extensively.

Study of the boundary layer and the investigation of the current discharge structure in the disk generator configuration were initiated. The computer codes to predict the performance of the disk generator experimental facility are being

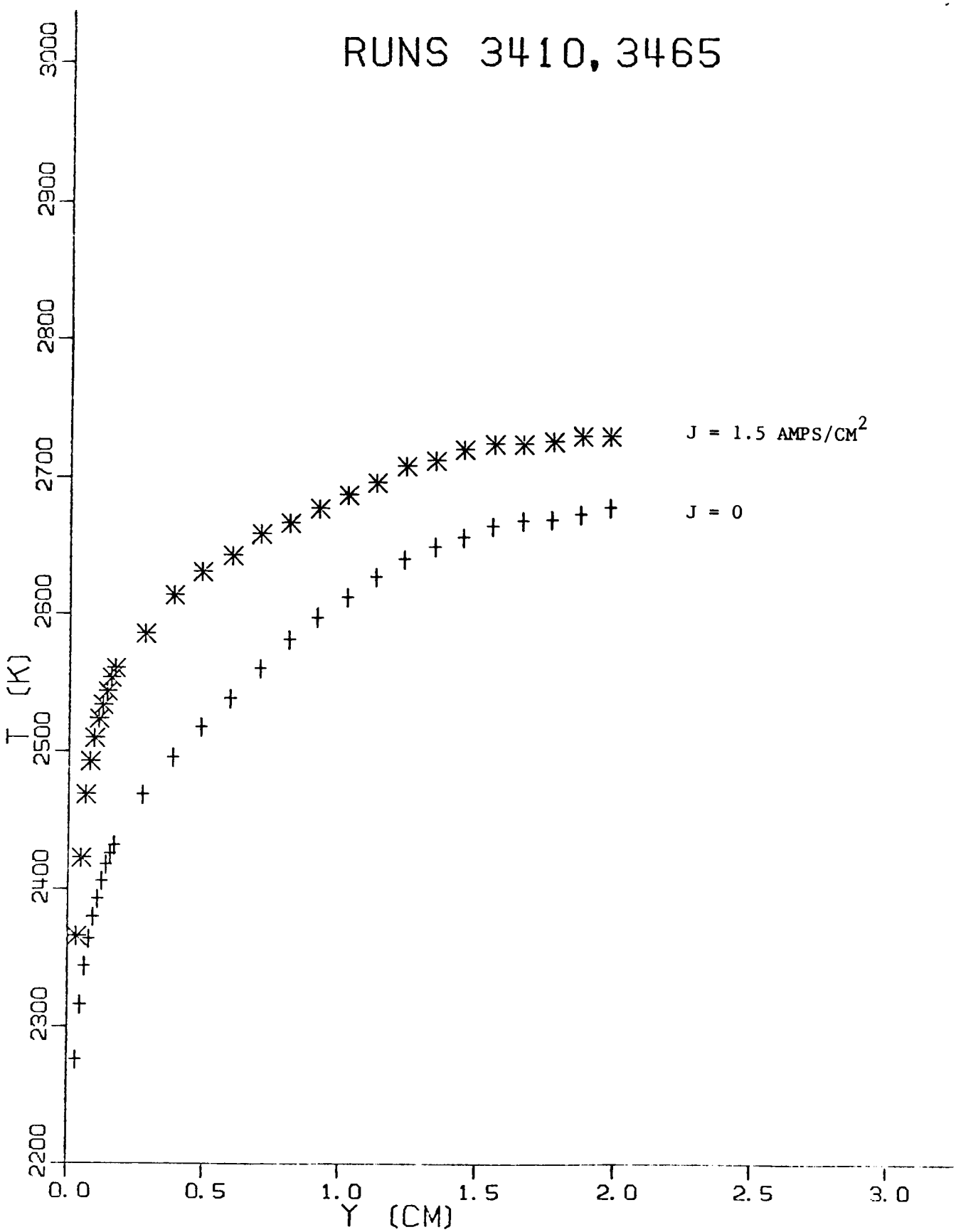


Figure 18. Comparison of Temperature Profiles with and without current.

developed. The study to predict the performance and to assess the applicability of the disk generator to the commercial MHD power plant was started.

Construction of the Disk Generator Experimental Facility

The main components of the disk generator experimental facility--the combustor, the plenum chamber and the disk generator test section with the water cooled cathode and anode--have undergone two series of thermal tests for a total operation time of 4 hours.

The disk generator insulation plates were constructed with metalyzed $M_gO$ ceramics that were brazed to the water cooled base plate for heat removal. $M_gO$ pieces (magnorite by Norton Co.) were coated with a copper layer of typically .005" thickness by means of a plasma spraying technique. The metalyzed surface was brazed to the 1/8" copper base plate which in turn was bolted to the water cooled test section housing. The brazing was done using $C_u/A_g/S_n$ or $C_u/A_g$ braze alloy in a vacuum furnace. Previously, brazing had been conducted in a hydrogen furnace until it was found that the hydrogen atmosphere at braze temperature ($780^oC$) caused deterioration of the structural integrity of the ceramics.

Figure 19 and Figure 20 show the latest disk generator insulator plates photographed before and after a series of thermal tests. The water cooled stainless steel anode is placed on the downstream insulator plate (Figure 19b). The water cooled copper cathode ring which had operated satisfactorily for the previous thermal test was not installed for this test. The insulator plate shown in Figure 20 underwent 2 1/2 hours of thermal tests with the mass flow rate of up to .11 $K_g/s$ of the alcohol/oxygen/nitrogen combustion gas. At this mass flow rate the Mach number at the inlet of the disk is about .43. From the signals of thermocouples imbedded in the $M_gO$ bricks, the surface temperature of the $M_gO$ brick and the heat flux at the inlet of the test section on the downstream insulator plate (Figure 20b) is estimated to be 2000 K and 78 watt/$cm^2$ respectively. At this condition the heat flux to the water cooled anode is 360 watt/$cm^2$.

After the thermal tests, the insulator plates were disassembled and examined in detail. The insulator plates were sectioned at various locations to examine the ceramic-metal interfaces. Figure 21 shows photographs of the insulator plate cross sections. At some locations the surface layer is sheared off from the bottom layer firmly attached to the copper plate. At other locations the ceramic-metal interface shows signs of deterioration, i.e., the separation of $M_gO$-plasma sprayed copper bond and/or the separation of the braze interface. The first deterioration, i.e. the surface layer shear off, is due to the high shear stress caused by the extremely high temperature gradient (~ 2500 K/cm) and the second deterioration is partly due to the combination of the thermal shear stress, the heating caused by high heat flux and partly due to the insufficient brazing. A microscope photograph of the ceramics-metal interface is shown in Figure 22.

Though the disk generator system operated at mass flow rates that are in the range of actual power generation experiments, further improvements of the test section are warranted for reliable thermal and electrical operations. Test sections constructed with $M_gO$ bricks attached to the copper base plate with a

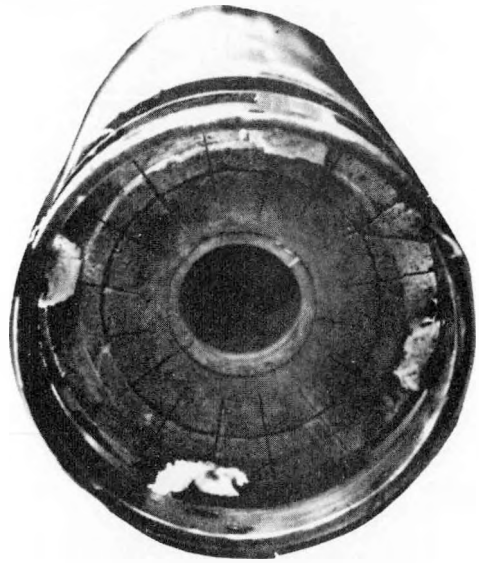

(a)

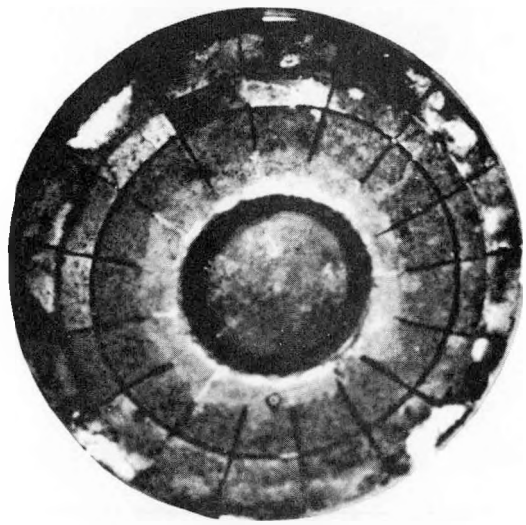

(b)

Fig. 19. Disk generator insulator plates, the upstream plate (a) and the downstream plate (b), before the thermal test. The water cooled stainless steel anode is placed on the downstream insulator plate (b).

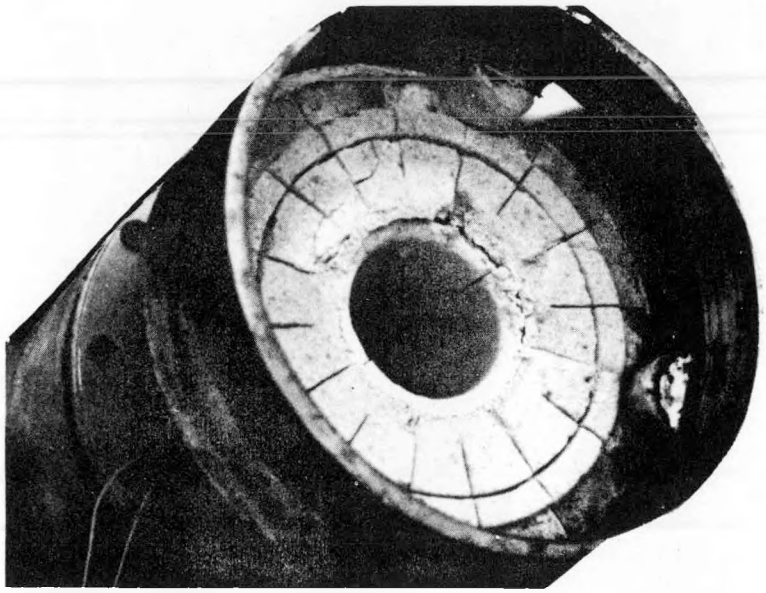

(a)

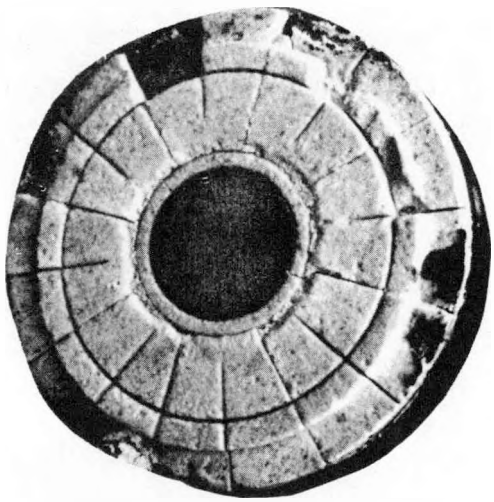

(b)

Figure 20. The disk generator insulator plates after 2 1/2 hours of thermal tests with mass flow rate of up to .11 kg/s of the alcohol/oxygen/nitrogen combustion gas.

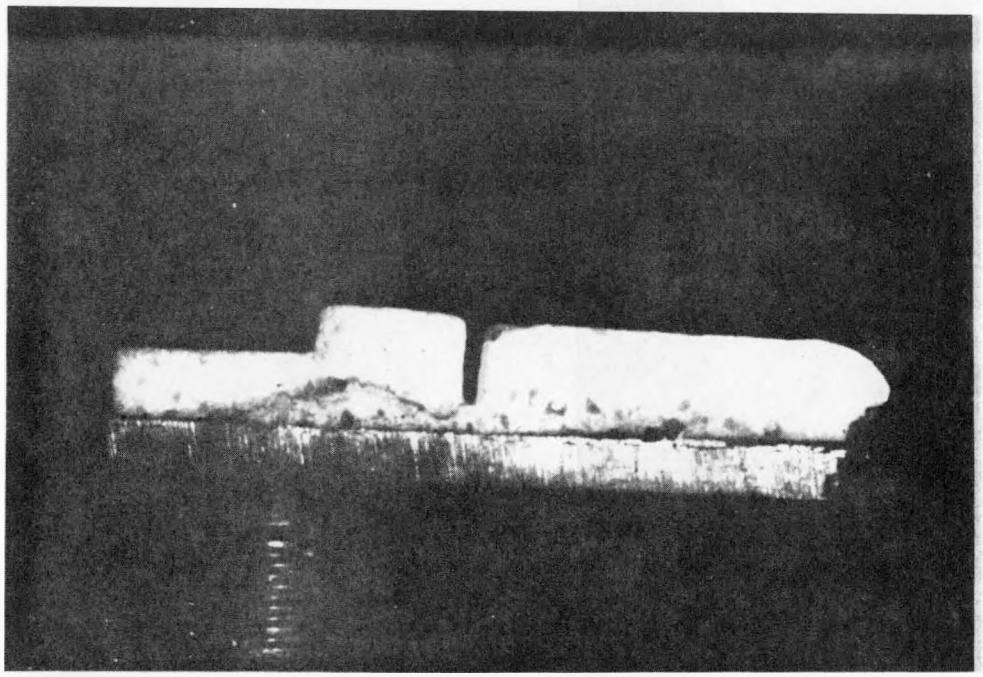

(a)

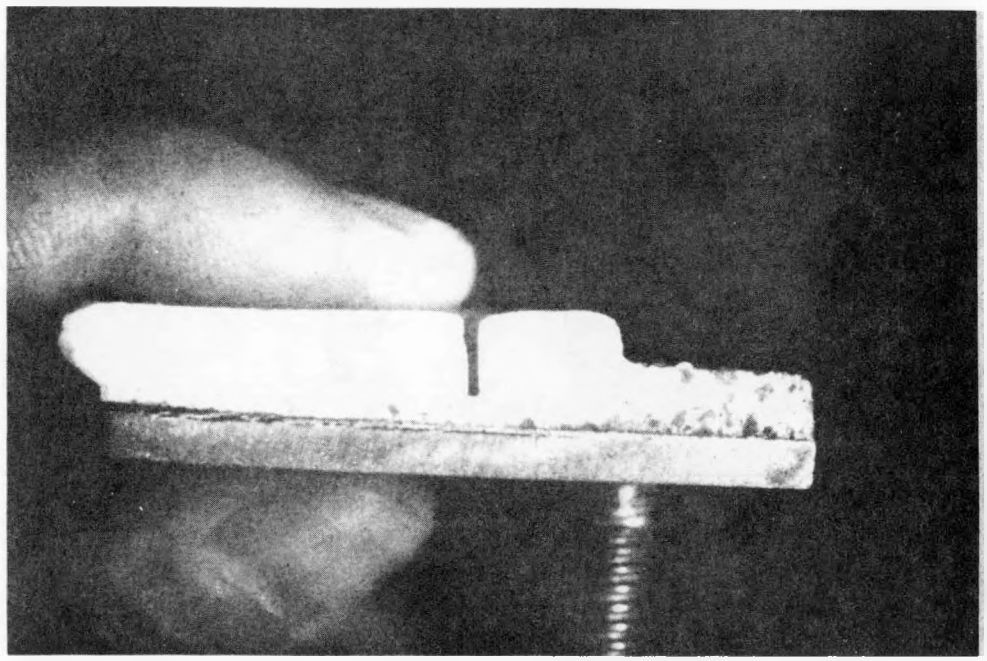

(b)

Figure 21. The disk insulator plate cross sections. The surface layer sheared off from the bottom layer (a) and the ceramic-metal interface shows signs of deterioration (b).

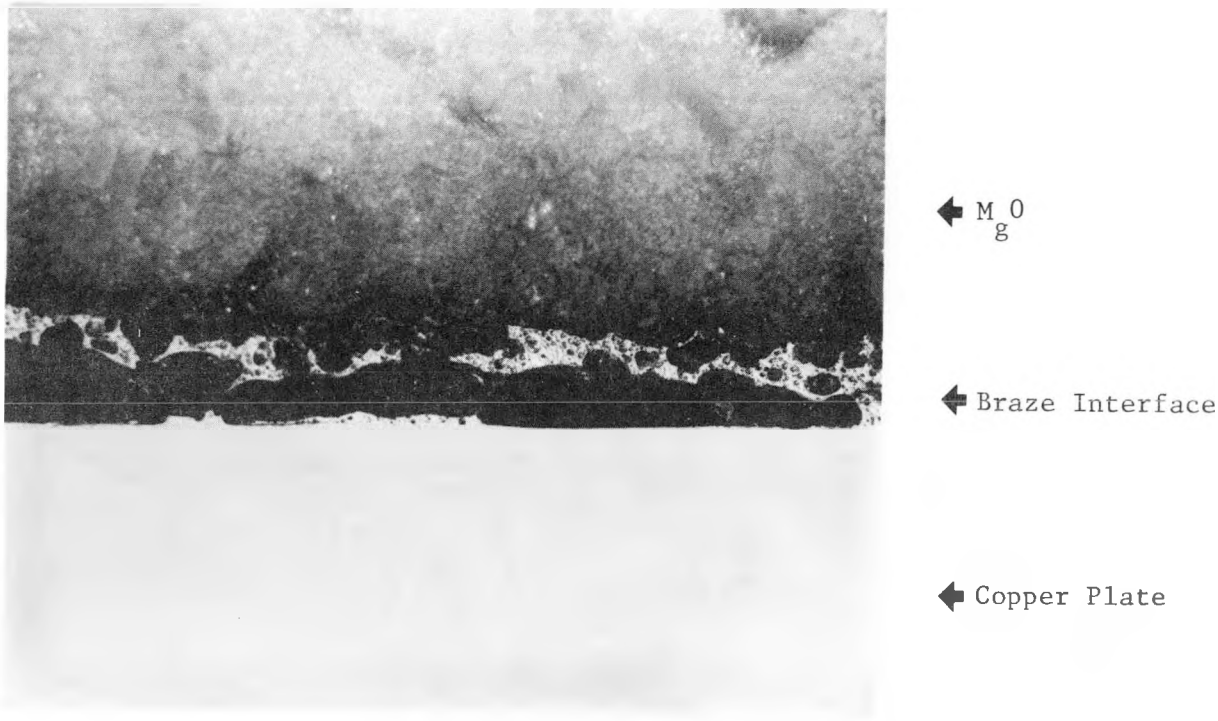


Figure 22. Microscope photograph (20X) of the ceramics-metal interface. The $M_gO$ ceramic texture, thin dark layer of plasma sprayed copper, grey braze material layer and large bubble-shaped voids are visible. The white area at the bottom half of the picture is the copper plate on which the $M_gO$ was brazed.

copper wire matt as a compliant layer will be tested. This structure would enable the ceramic plate to expand freely and thereby relieve thermal shear stress between the ceramics and the copper base plate.

Boundary Layer Study

The boundary layers in the disk generator represent an area where considerable work is needed. The flow undergoes a rapid expansion in the presence of an adverse pressure gradient. The analysis of boundary layers in the presence of adverse pressure gradients is incomplete and rather poorly understood. Useful predictive tools are not as readily available as they are in the case of flows with favorable or negligible pressure gradients. The similarities of the flow in the disk generator to that of a radial outflow vaneless diffuser have been noted and have led to an investigation into research on radial diffusers.

A review of the literature of radial diffusers has disclosed that the boundary layer problem in radial diffusers is poorly understood. The designer of turbomachinery is primarily interested in friction and associated losses; the majority of the work surveyed serves to predict such parameters as friction and loss coefficients, while doing relatively little to examine the boundary layer itself in any great detail. Typically a flat-plate zero pressure gradient analysis is used, with a friction factor adjusted upwards to match the experimental data. A similar procedure has also been used in MHD work as well, including earlier numerical studies of the disk generator [4].

The next level of analysis used integral boundary layer models, which have proven useful for predicting wide classes of flows. The governing equations of the problem are written in differential form, including terms containing the boundary layer effects. Then a velocity profile is assumed and the partial differential equations integrated in the direction normal to the wall, leaving ordinary differential equations. Experimental data is relied on to obtain suitable velocity profiles and empirical expressions for the friction terms.

In a theoretical and experimental study by Jansen [5], the following expressions are proposed for the radial and tangential velocity profiles:

$$V_\theta(r,z) = \left(\frac{z}{\delta}\right)^{1/10} V_\theta \qquad 0 \le z \le \delta \quad \text{(boundary layer)}$$

$$V_\theta(r,z) = V_\theta \qquad \delta \le z \le h/2 \quad \text{(inviscid core)}$$

$$V_r(r,z) = \left\{1 - \left(\frac{2\delta}{h}\right)\left(1 - \frac{z}{\delta}\right)^2\right\}\left(\frac{z}{\delta}\right)^{1/10} V_{r(r)} \qquad 0 \le z \le \delta$$

$$V_r(r,z) = V_r \qquad \delta \le z \le h/2$$

where $V_r$ and $V_\theta$ represent core values of radial and tangential velocities and $h$ is the channel height. The boundary layer thickness $\delta$ acts as a shape factor. Various velocity profiles are plotted in Figure 23 for a

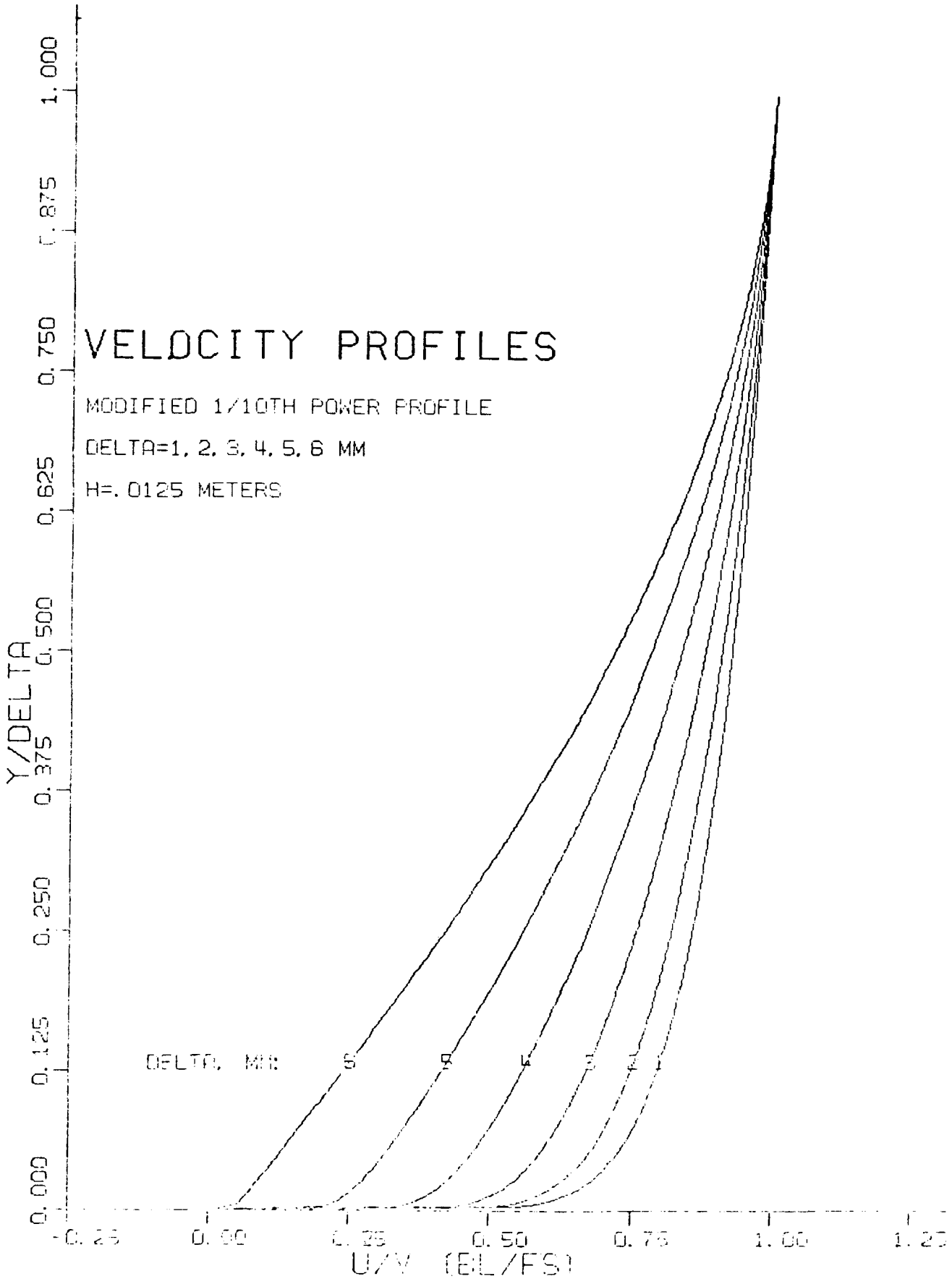


Figure 23. Velocity Profiles

channel height of 1.25 cm, and the boundary layer thickness as a parameter. It can be seen that as the boundary layer grows, the slope of the velocity profile near the wall is tending towards zero, indicating separation. It is felt that this profile is suitable only for the entry length region, since it predicts separation when $\delta=h/2$. Ordinary flat-plate values of the boundary layer thickness in the Stanford disk generator indicate a thickness of about 1 mm (for a channel height of 1.25 cm), which is in the range of the forming boundary layer region. This is also in the region where the more complex boundary layer profile proposed by Jansen collapses to the simpler more common 1/7th power law profile.

The next phase of this investigation will be a comparison of this more complicated velocity profile with the simpler power law. Integration of the modified power law profile results in much more complicated expressions for the governing equations, and it is hoped that this study will indicate whether or not the simpler expression is suitable.

Current Discharge Study

Current discharge in the disk generator is subject to different constraints from those of the linear generator. The azimuthal current closes upon itself, thereby eliminating electrodes sustaining induced current. The lack of electric field in the azimuthal direction simplifies the structure of the insulator wall as the insulation must be made only in the radial direction. The most important characteristic, however, is that the current flows along the applied magnetic field when it goes into or emerges from the electrodes. This is fundamentally different from the current discharge configuration of linear generators and is an important advantage of the disk generator regarding the life time of the electrode or inter-electrode break down phenomena.

In order to comprehend the current discharge configuration in the disk geometry, a numerical analysis of the current distribution in the disk generator was initiated. For the cylindrical coordinate system pertinent to the disk geometry, Maxwell's equations, the quasi-neutrality equation and Ohm's law yield the partial differential equation of the elliptic type for the current stream function $\psi$ and the potential function $\phi$ as

$$\frac{\partial^2\psi}{\partial r^2} + (1+\beta^2)\frac{\partial^2\psi}{\partial z^2} - \left(\frac{\partial \ln \sigma}{\partial r} + \frac{1}{r}\right)\frac{\partial\psi}{\partial r} + \sigma\left[\frac{\partial}{\partial z}\left(\frac{1}{\sigma_\beta}\right)\right]\frac{\partial\psi}{\partial z}$$

$$- \sigma r \frac{\partial}{\partial z}(V_\theta B + \beta V_r B) = 0$$

$$\frac{\partial^2\phi}{\partial r^2} + (1+\beta^2)\frac{\partial^2\phi}{\partial z^2} + \left(\frac{\partial \ln \sigma_\beta}{\partial r} + \frac{1}{r}\right)\frac{\partial\phi}{\partial r} + \left[(1+\beta^2)\frac{\partial \ln \sigma}{\partial z}\right]\frac{\partial\phi}{\partial z}$$

$$- \left[\frac{\partial \ln \sigma_\beta}{\partial r} + \frac{1}{r}\right](V_\theta B + \beta V_r B) - \frac{\partial}{\partial r}(V_\theta B + \beta V_r B) = 0$$

where

$$j_r = \frac{1}{r}\frac{\partial\psi}{\partial z}, \quad j_z = \frac{1}{r}\frac{\partial\psi}{\partial r}$$

$$E_r = -\frac{\partial \phi}{\partial r} \quad , \quad E_z = -\frac{\partial \phi}{\partial z}$$

and

$$\sigma_\beta = \frac{\sigma}{1+\beta^2}$$

It is to be noted that the azimuthal current $j_\theta$ does not appear explicitly in the above equations due to the condition

$$\frac{\partial}{\partial \theta} = 0.$$

The above equations can be solved by the finite difference method, provided theomodynamic and electric properties are specified at each grid point. A preliminary solution of the partial differential equation for $\psi$ is given in Figure 24. For this trial solution

$$\frac{\partial}{\partial z} = 0$$

is assumed. Thermodynamic and electrical properties along the radial direction are given by the core flow calculation reported in the previous quarterly report (Quarterly Progress Report April-June, 1977, Figure 21). It is shown in Figure 24 that the Hall current stream lines emerge from the anode surface without concentration and fill the test section uniformly. At the cathode surface current recirculation is observed and the load current is shifted to the downstream end of the cathode. The current recirculation over the cathode surface is due to the large cathode surface area. The method of the solution will be improved to take into account the boundary layer effect and more realistic generator geometries.

Performance Prediction Study

During the last quarter the effort has been focused on two areas--performance prediction of the disk generator experimental facility and the assessment of the disk generator to the commercial MHD power plant.

As for the performance prediction of the disk generator experimental facility, studies were undertaken to examine the effect of plasma inlet conditions and magnetic field strengths on the power output of the disk generator. This study was carried out using a performance prediction program that is being developed in conjunction with the experimental work on the disk generator. Input parameters that were varied were: mass flow rate, magnetic field strength, inlet static temperature, inlet tangential velocity (swirl), and load current. A constant height channel was used with z=1.25 cm. The inlet static radius was 5 cm and the exit radius was 8 cm. The inlet static pressure in all cases was 1 atm. Plasma properties were evaluated from calculated equilibrium concentrations using an existing properties subroutine. The inlet swirl velocity was varied as a specified percentage of the inlet radial velocity. There were no friction or heat transfer effects included in this analysis.

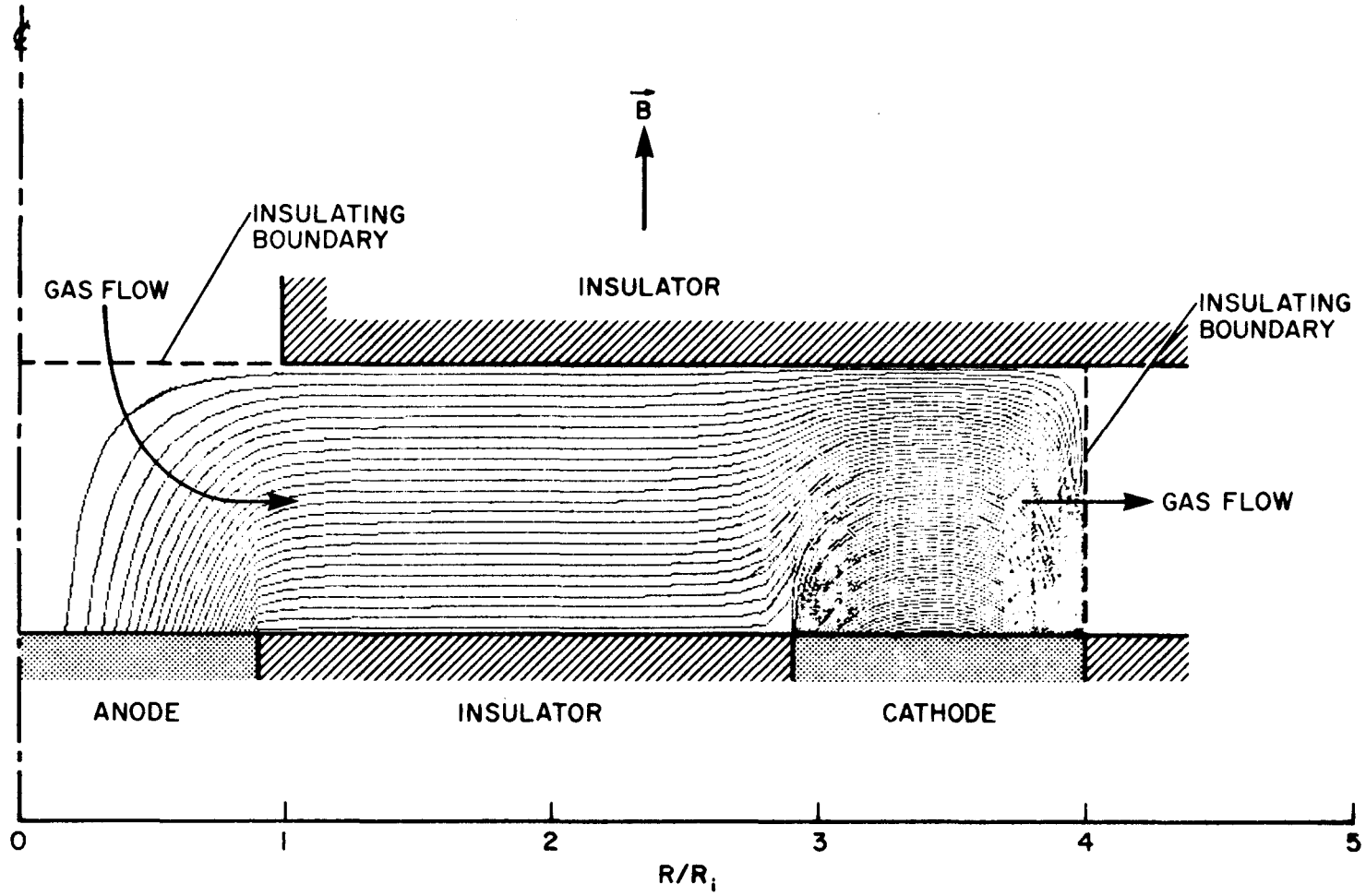


Figure 24. A trial solution of the partial differential equation governing the Hall current stream line. $\partial/\partial z = 0$ is assumed. Thermodynamic and electrical properties of the gas flow are those reported in the previous quarterly report (Quarterly Progress Report April-June, 1977, Fig. 21).

# TEMPERATURE EFFECTS

B=6 TESLA
M=.2 KG/SEC
P=1 ATM (INLET)

RI=5 CM
RO=8 CM
Z=1.25 CM

CASE 1: T=2400 K
CASE 2: T=2600 K
CASE 3: T=2800 K

SWIRL=0, 25, 50, 75, 100% OF INLET VELOCITY

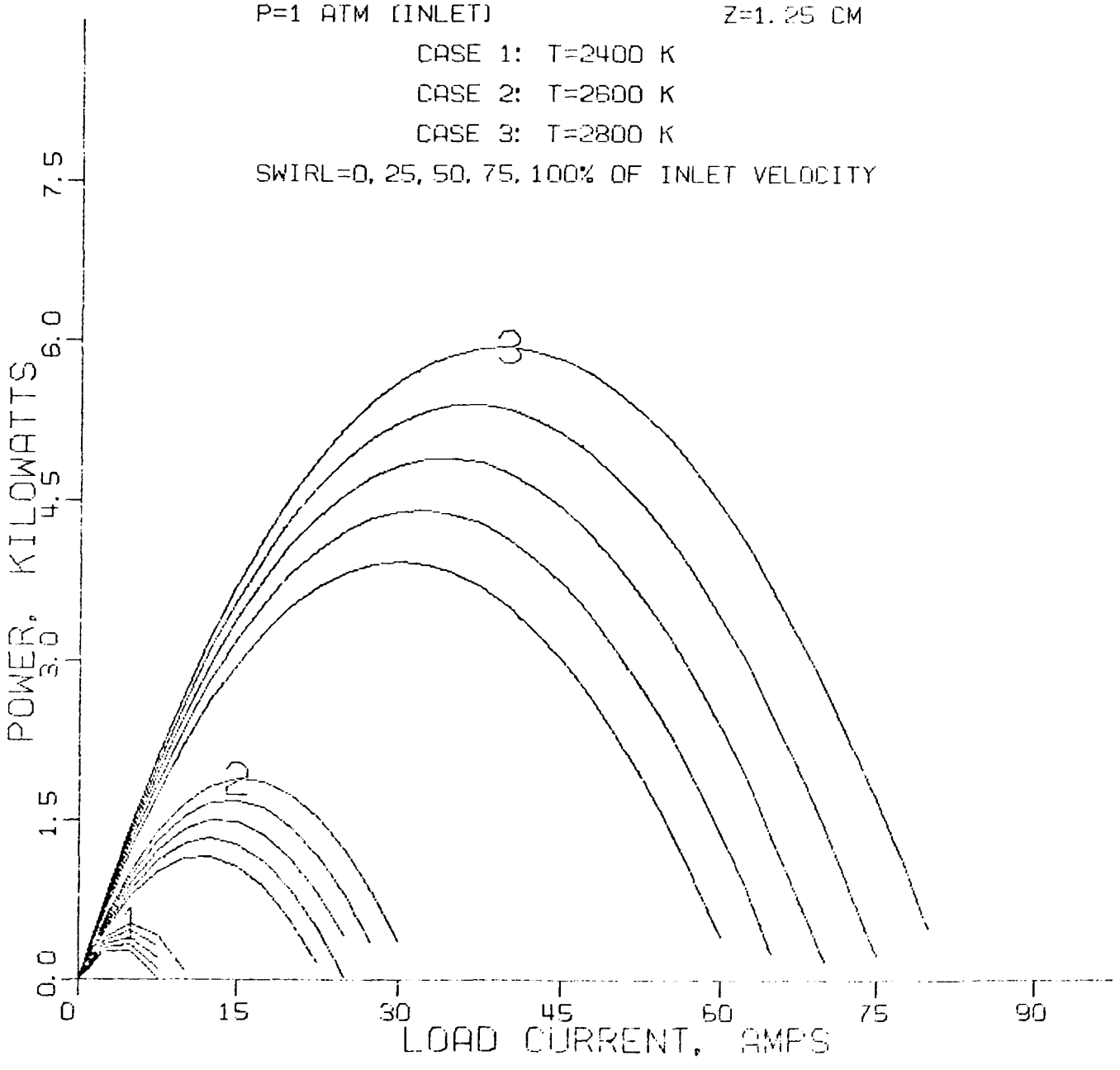


Figure 25. Temperature Effects

# MAGNETIC FIELD EFFECTS

T=2800 K RI=5 CM
M=.2 KG/SEC RO=8 CM
P=1 ATM (INLET) Z=1.25 CM
CASE 1: B=2 TESLA
CASE 2: B=4 TESLA
CASE 3: B=6 TESLA
SWIRL=0, 25, 50, 75, 100% OF INLET VELOCITY

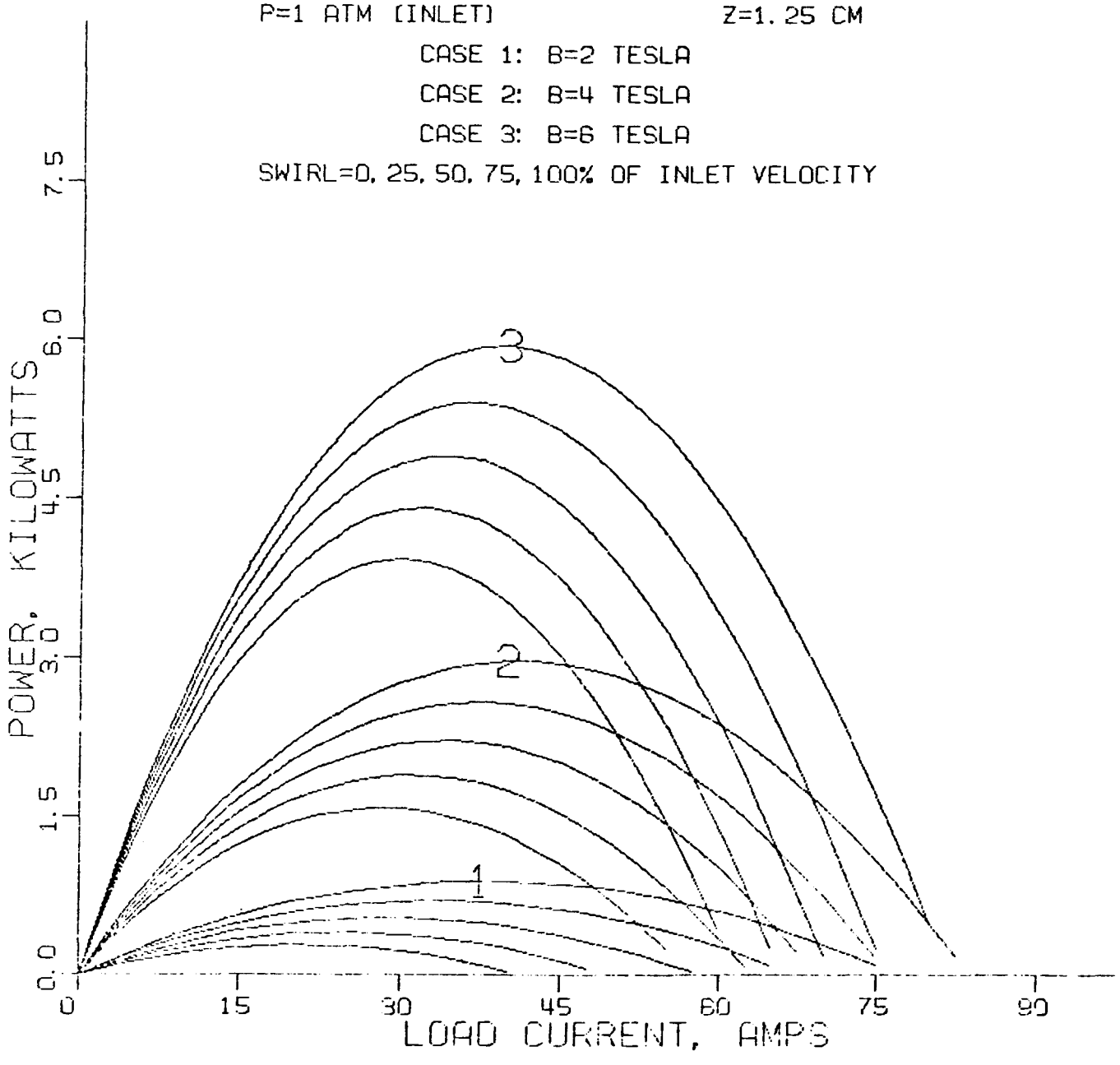


Figure 26. Magnetic Field Effects

# MASS FLOW RATE EFFECTS

B=6 TESLA RI=5 CM
T=2800 K RO=8 CM
P=1 ATM (INLET) Z=1.25 CM
CASE 1: M=.1 KG/SEC
CASE 2: M=.15 KG/SEC
CASE 3: M=.2 KG/SEC
SWIRL=0, 25, 50, 75, 100% OF INLET VELOCITY

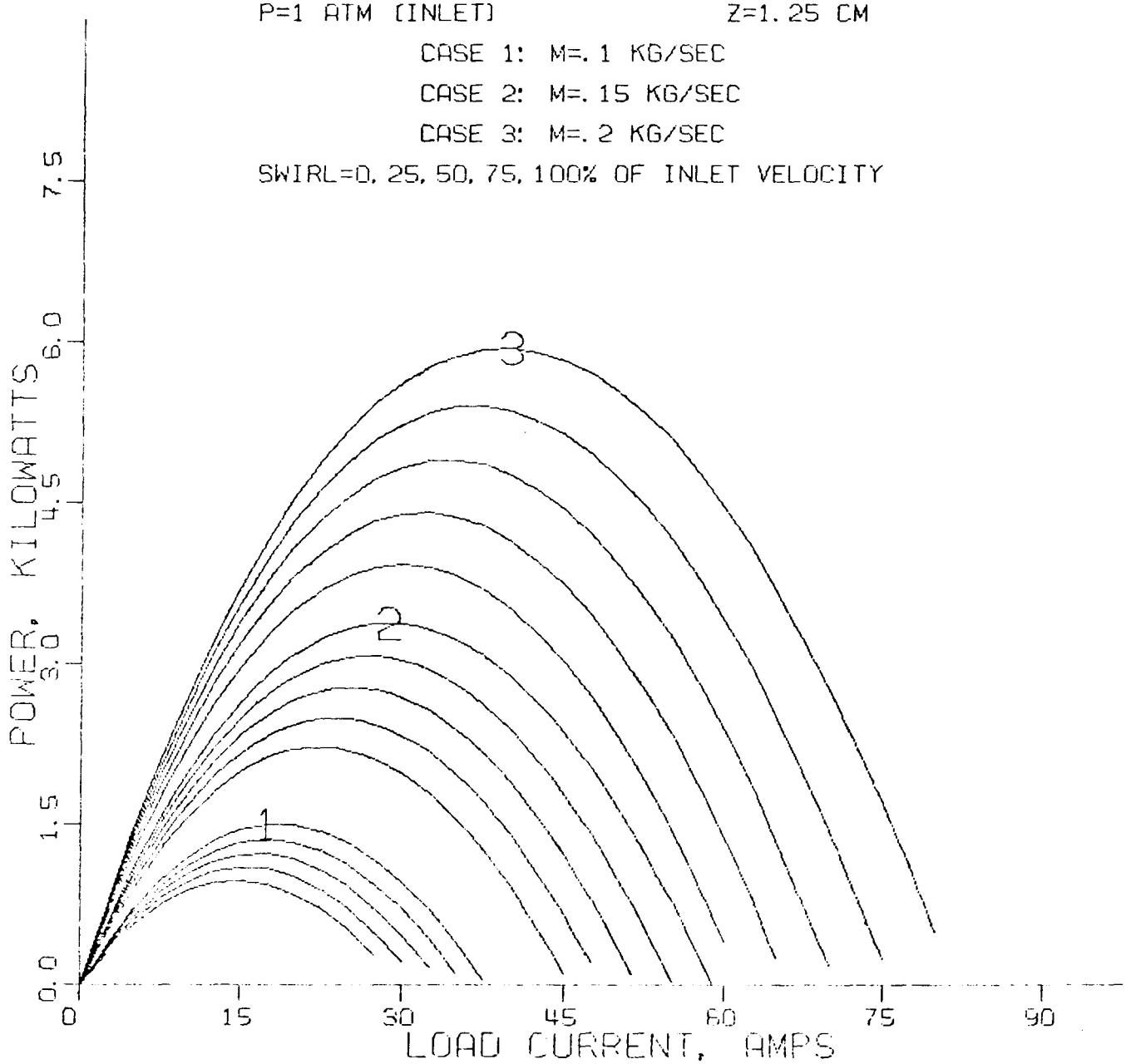


Figure 27. Mass Flow Rate Effects

Some characteristic results are presented in Figure 25. The output power is plotted as a function of load current for various input parameters. Each plot contains three different values of the variable of interest, and within each flow case there are five lines, indicating the effect of swirl within that case. The lower line in each group refers to the case with no swirl, with the increasing values of power corresponding to 25,50,75, and 100% inlet swirl. The marked increase of power output by small changes in inlet static temperature and the enhancement of the incremental increase in power output by swirl at high temperatures are illustrated in the Figure

Figure 26 and Figure 27 show the increase in power output for increases in magnetic field strength and for the increase of the mass flow rate respectively. Again it is apparent that the effects of swirl are enchanced at higher magnetic fields. It should also be noted that the effect of swirl is much more pronounced near short-circuit conditions. This is where the radial current densities are highest, and therefore the JxB body force in the negative swirl direction has a much greater effect, tending to induce a rotation in the plasma which degrades the performance of the machine. Therefore the introduction of a counteracting positive swirl component has a greater effect near short circuit than at open circuit. This evident in the other cases as well.

Progress has been made to develop computer codes to predict the performance of the disk generator for high enthalpy extraction. These codes compute the local thermodynamic and electrical properties of the core flow along the radial direction and determine the geometrical configulation of the channel according to the prescribed enthalpy extration mode. To date a number of different modes have been analyzed for the conditions pertinent to the combustion driven MHD generator. The study will be continued to delineate criteria for high enthalpy extraction at acceptable turbine efficiencies and to assess the applicability of the disk generator for the commercial MHD power plant.

### 3.3.2 Peg Wall Tests

Work this quarter again centered around channel design. Tests were conducted to test the peg wall concept, a channel configuration was decided upon, and a preliminary test was conducted on a possible electrode material.

In order to confirm the thermal and electrical integrity of the peg wall design concept (see Reference [6]), two sets of tests were run. The first tests used an acetylene torch as the heat source. These tests were successful in that all pegs and the G-10 supporting layer remained intact and the desired heat flux of 100 $W/cm^2$ was achieved. To further test the design, the peg wall assembly was modified for tests with Stanford's M-2 combustor in a simple channel.

In the M-2 tests the thermal performance of the assembly was more than adequate. The peg surface temperature was held above 2200 K with an associated heat flux of 175 $w/cm^2$. The assembly after these tests is shown in Figure 28. As a part of these tests 1% potassium seed was introduced into the flow and a voltage was applied to adjacent pegs. Current leakage was detected as seed apparently penetrated the castable ceramic, a variation of Norton's Magnorite CM 364. This problem and possible solutions are currently being studied.

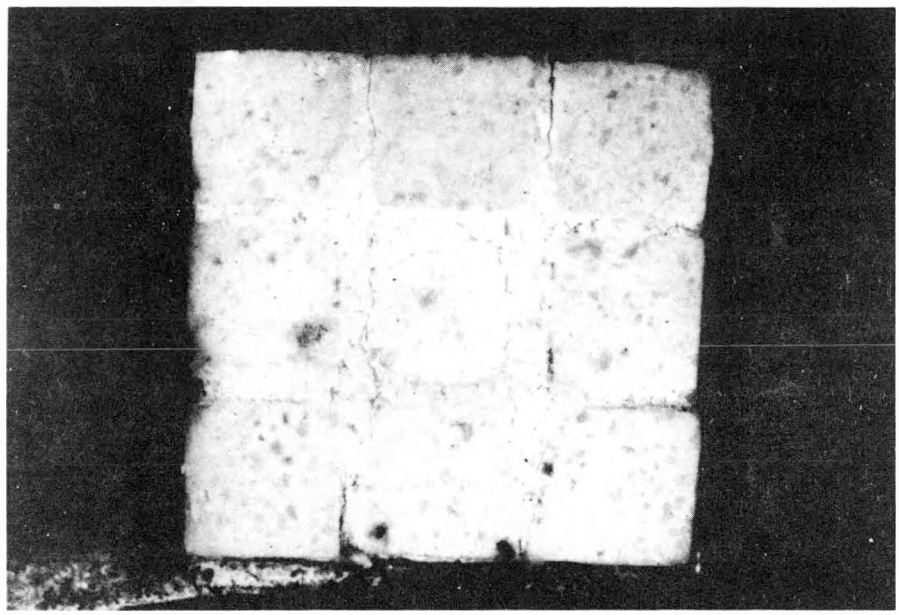

Figure 28. Post Test Pegwall Assembly

## Computer Studies

As earlier reported, changes were needed to use ONED, a one-dimensional MHD core code, as a design tool. To date, ONED has been changed to give acceptable results for design of the linear channel in the small 6 Tesla magnet. Work continues to improve the treatment of the boundary layer so the code will be useful in more general situations.

## Test Section Design

The first use of ONED as a design tool was to aid in the choice of the test section configuration. The three general configurations shown in Figure 29 were considered. Of these three the analysis indicated the large straight channel would provide the most favorable conditions for our investigations. More detailed design work has begun using this configuration.

## Electrodes

Due to the small space available in the superconducting magnet and the relatively long lead-in length, approximately .4 m to the test section, boundary layer effects are important. To decrease the associated effects including electrode voltage drops it has been decided to investigate the use of hot electrodes. Of the materials available $La\ Mg_{.05}\ Cr_{.95}\ O_3$ was chosen.

In conjunction with the peg wall tests with the M-2 combuster 2.25 cm x .5 cm electrodes of lanthanum-chromite were placed in the channel. The results of the test were promising as the electrodes operated at temperatures up to 2000 K and current densities well above 1 amp/$cm^2$. Figure 30 shows the anode after the test. Further tests are planned with these electrodes to develop a better attachment of the ceramic to a metal base. Dr. Barry Rossing of the Westinghouse Corporation was very helpful in supplying samples of the lanthanum-chromite material.

a) Large Straight Test Section

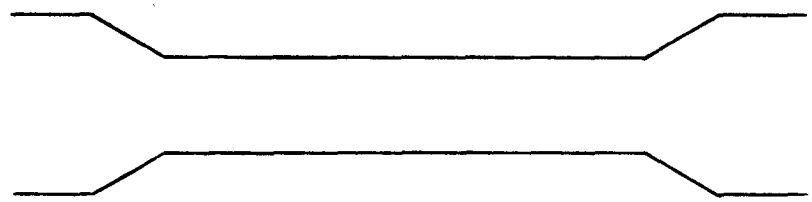

b) Small Straight Test Section

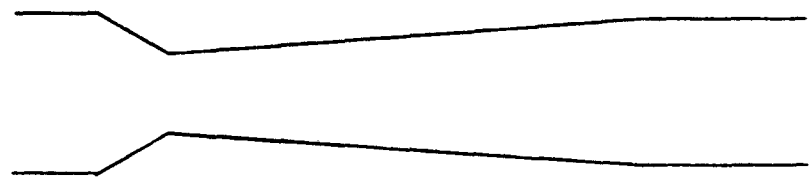

c) Diverging Test Section

Figure 29. ONED Comparison Channel Configurations

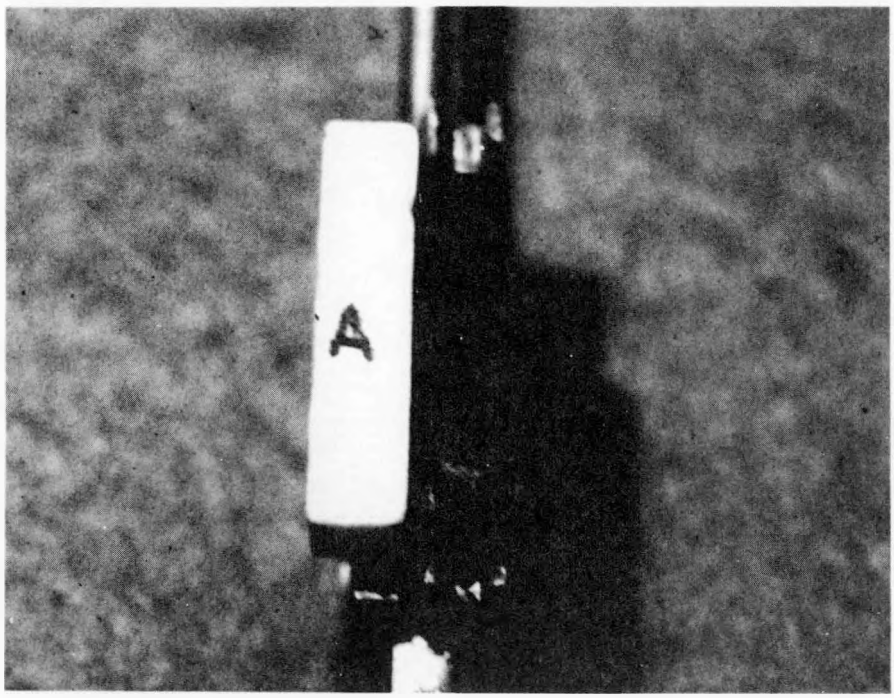


Figure 30. Post Test Anode

## 4.0 REFERENCES


[1] Lijnse, P.L. and Hornman, J.C., J. Quant. Spectrose. Radiat. Transfer, 14, 1079 (1974).

[2] Daily, J. W., "Boundary Layer Phenomena in Combustion-Driven MHD Power Generators," HTGL Report No. 102, December 1975.

[3] Olin, J. G., "Turbulence Suppression in Magnetohydrodynamic Flows," SU-IPR Report No. 85, July 1966.

[4] Louis, J. F., "Disk Generator," AIAA, 6, No. 9., Sept., 1968, pp. 1674-1678.

[5] Jansen, W., "Steady Flow in a Radial Vaneless Diffuser," Trans ASME. D, September 1964, pp. 607-619.

[6] ERDA, Annual Report for the Period July, 1976 - June, 1977, Contract No. EX 76-C-01-2341, Report No. FE-2341-3, July, 1977.




☆U.S. GOVERNMENT PRINTING OFFICE: 1978-740-206/22